

Selective Laser Melting of H13 Tool Steel for Rapid Tooling

by  
Michael Katancik

A THESIS

submitted to  
Oregon State University  
Honors College

in partial fulfillment of  
the requirements for the  
degree of

Honors Baccalaureate of Science in Mechanical Engineering  
(Honors Scholar)

Presented March 12, 2019  
Commencement June 2019



## AN ABSTRACT OF THE THESIS OF

Michael Katancik for the degree of Honors Baccalaureate of Science in Mechanical Engineering presented on March 12, 2019. Title: Selective Laser Melting of H13 Tool Steel for Rapid Tooling.

Abstract approved: \_\_\_\_\_  
Somayeh Pasebani

The current knowledge on the microstructural evolutions and mechanical properties of selective laser melting (SLM) produced H13 tool steel components is limited. This research is focused on optimization of SLM processing parameters for H13 tool steel and investigation of microstructure and mechanical properties of H13 tool steel components after SLM and heat treatment. H13 components with a relative density of ~99% were additively manufactured using the SLM process. The highest density part (relevant density 99%) with the lowest level of porosity (<0.01%) was made with a volumetric energy density (VED) of 760 J/mm<sup>3</sup> (152 W laser power, 100 mm/s scanning speed, 40μm hatch spacing, and 50 μm layer thickness). Wrought and SLM produced samples underwent tempering at 550, 600, and 650°C for two hours followed by furnace cooling. Both SLMed samples and austenitized followed by water quenched wrought samples presented martensitic microstructures with similar microhardness values of ~708 HV. No obvious trend was observed between VED and microhardness values. SLMed and tempered samples showed high microhardness value of 728.5±28.2 HV due to presence of high dislocation density caused by rapid solidification during SLM, finer grains and microstructure, and precipitation of second phase (carbides) during tempering. Tempered martensitic structure was observed in SLMed and tempered samples. These precipitates showed coarsening at 600 and 650°C leading to a decrease in microhardness. SLMed samples maintained higher microhardness values than wrought H13 samples at each tempering temperature likely due to higher dislocation density and finer

grains present in SLMed parts (rapid solidification characteristics). High relative densities (99.9% or greater) were not achieved in SLMed parts, and further optimization deemed necessary to achieve full density parts. Furthermore, presence of cracks in the SLMed H13 tool steel parts is a problem that needs to be addressed before implementation of SLMed molds in applications that require high thermal fatigue resistance such as like plastic injection molding.

Key Words: additive manufacturing, selective laser melting, H13 tool steel, rapid tooling, powder bed fusion, injection molding, rapid solidification

Corresponding e-mail address: [katancim@oregonstate.edu](mailto:katancim@oregonstate.edu)

©Copyright by Michael Katancik  
March 12, 2019

Selective Laser Melting of H13 Tool Steel for Rapid Tooling

by  
Michael Katancik

A THESIS

submitted to  
Oregon State University  
Honors College

in partial fulfillment of  
the requirements for the  
degree of

Honors Baccalaureate of Science in Mechanical Engineering  
(Honors Scholar)

Presented March 12, 2019  
Commencement June 2019

Honors Baccalaureate of Science in Mechanical Engineering project of Michael Katancik  
presented on March 12, 2019

APPROVED:

---

Somayeh Pasebani, Mentor, representing Mechanical, Industrial, and Manufacturing Engineering

---

Zhaoyan Fan, Committee Member, representing Mechanical, Industrial, and Manufacturing Engineering

---

Ali Tabei, Committee Member, representing Mechanical, Industrial, and Manufacturing Engineering

---

Toni Doolen, Dean, Oregon State University Honors College

I understand that my project will become part of the permanent collection of Oregon State University, Honors College. My signature below authorizes release of my project to any reader upon request.

---

Michael Katancik, Author

## Acknowledgements

There are many people I'd like to thank for making this research study possible. First and foremost, a thank you to Dr. Somayeh Pasebani for her time, effort and guidance. Additionally, I'd like to thank Dr. Zhaoyan Fan and Dr. Ali Tabei for being a part of my committee and taking an interest in my research pursuits. I am also grateful for Milad Ghayoor being so patient and spending more time than necessary teaching me the metallography and XRD process.

Without Oregon Manufacturing Innovation Center (OMIC) this project would never have had a place to start and I am happy I was able to be a part of OMIC Rapid Tooling Project Team. I'm glad ATAMI is open 24/7 and equipped with state of the art facilities, so thank you to the entire staff for operating such a great research facility available to college of engineering students. In particular I'd like to thank Neill Thornton for teaching me the ways of the box furnace and making sure all our equipment and facilities are in peak condition.

Outside of ATAMI I also would like to thank Teresa Sawyer from the OSU Electron Microscopy Facility for capturing the SEM images used in this study and Brian Jensen for providing guidance and access to the necessary tools in the MIME Machining and Product Realization Laboratory. I'd also like to thank Alyssa Pautsch for her extended efforts to help acquire our necessary materials.

Finally, I'd like to thank the Honors College for providing the thesis process and financial support in accomplishing my research goals. The college and staff were generous in their time and funding associated with my project.

## Dedication

I would like to dedicate this project to my parents for always being supportive and loving in everything I do. I wouldn't have gotten this far without you two! Thanks Mom and Dad.

## Table of Contents

|       |                                           |    |
|-------|-------------------------------------------|----|
| 1     | Introduction.....                         | 19 |
| 2     | Literature Review .....                   | 21 |
| 2.1   | Plastic Injection Molding .....           | 21 |
| 2.1.1 | Plastic Injection Molding Process.....    | 21 |
| 2.1.2 | Injection Molding Tooling Features .....  | 22 |
| 2.1.3 | Tooling Production .....                  | 25 |
| 2.2   | Types of Additive Manufacturing (AM)..... | 28 |
| 2.2.1 | Material Extrusion.....                   | 28 |
| 2.2.2 | Direct Energy Deposition.....             | 31 |
| 2.2.3 | Powder Bed Fusion .....                   | 34 |
| 2.3   | Selective Laser Melting.....              | 34 |
| 2.3.1 | Powder Spreading Techniques .....         | 36 |
| 2.3.2 | Chamber Conditions.....                   | 36 |
| 2.3.3 | Deposition Rate.....                      | 37 |
| 2.4   | SLM Processing Parameters.....            | 38 |
| 2.4.1 | Laser Power .....                         | 38 |
| 2.4.2 | Laser Scanning Speed .....                | 38 |
| 2.4.3 | Layer Thickness .....                     | 39 |
| 2.4.4 | Volumetric Energy Density .....           | 39 |

|       |                                                                       |    |
|-------|-----------------------------------------------------------------------|----|
| 2.4.5 | Laser Energy Density .....                                            | 40 |
| 2.4.6 | Hatch Spacing .....                                                   | 40 |
| 2.5   | Selective Laser Melting Machines .....                                | 40 |
| 2.5.1 | ORLAS Creator .....                                                   | 41 |
| 2.6   | H13 Tool Steel .....                                                  | 43 |
| 2.6.1 | Wrought Properties of H13 .....                                       | 43 |
| 2.6.2 | Microstructure of Additively Manufactured H13 Tool Steel .....        | 46 |
| 2.6.3 | Mechanical Properties of Additively Manufactured H13 Tool Steel ..... | 49 |
| 2.7   | Background Review .....                                               | 54 |
| 3     | Materials and Methods .....                                           | 55 |
| 3.1   | H13 Powder Feedstock for SLM Process .....                            | 55 |
| 3.1.1 | Morphology of H13 Powder .....                                        | 55 |
| 3.1.2 | Particle Size Distribution Analysis .....                             | 56 |
| 3.1.3 | Density Measurement .....                                             | 56 |
| 3.2   | Wrought H13 .....                                                     | 59 |
| 3.2.1 | Homogenizing Wrought H13 .....                                        | 59 |
| 3.3   | SLM Processing Parameters .....                                       | 60 |
| 3.3.1 | SLM Matrix .....                                                      | 60 |
| 3.3.2 | 3D Design of Test .....                                               | 61 |
| 3.3.3 | Density Measurement of SLMed H13 .....                                | 63 |

|       |                                           |    |
|-------|-------------------------------------------|----|
| 3.3.4 | Microstructure Characterization .....     | 64 |
| 3.4   | Tempering Heat Treatment .....            | 70 |
| 3.4.1 | Heat Treatment Method and Groups.....     | 71 |
| 4     | Results and Discussion .....              | 72 |
| 4.1   | Powder Morphology .....                   | 72 |
| 4.2   | Particle Size Distribution .....          | 73 |
| 4.3   | Powder Feedstock Density .....            | 75 |
| 4.3.1 | Apparent Density .....                    | 75 |
| 4.3.2 | Tap Density.....                          | 76 |
| 4.4   | Manufactured Part Density.....            | 77 |
| 4.5   | Microstructural Characterization.....     | 79 |
| 4.5.1 | Porosity Analysis .....                   | 80 |
| 4.5.2 | Microstructure and Grain Analysis.....    | 82 |
| 4.6   | Mechanical Properties.....                | 87 |
| 4.6.1 | Microhardness.....                        | 87 |
| 5     | Summary and Conclusions.....              | 90 |
| 6     | Current Limitations and Future Work ..... | 93 |
| 7     | References.....                           | 94 |

## List of Figures

|                                                                                                                                       |    |
|---------------------------------------------------------------------------------------------------------------------------------------|----|
| Figure 1: A diagram of a typical reciprocating screw injection molding machine [4].....                                               | 22 |
| Figure 2: A pie chart showing typical percentages of time spent for each portion of the injection molding process [1].....            | 23 |
| Figure 3: Straight cooling channels presented in both sides of an injection molding tool [10]....                                     | 24 |
| Figure 4: Conformal cooling channels presented in both sides of an injection molding tool [10]                                        | 25 |
| Figure 5: Schematic of a FFF machine nozzle [21].....                                                                                 | 29 |
| Figure 6: Desktop Metal Studio+ printer [26].....                                                                                     | 30 |
| Figure 7: A worm gear printed using Desktop Metal’s Studio series of additive manufacturing equipment [27].....                       | 31 |
| Figure 8: DED machine using a powder feeding system [29] .....                                                                        | 32 |
| Figure 9: The Optomec LENS® 450 system [31].....                                                                                      | 32 |
| Figure 10: DED used to repair a turbine blade where the (a) undamaged part and (b) the repaired part are presented [29].....          | 33 |
| Figure 11: A powder bed fusion machine diagram [34].....                                                                              | 34 |
| Figure 12: A titanium alloy aerospace component in an SLM chamber upon completion [36]...                                             | 35 |
| Figure 13: SLM manufactured motor cooling hub for an SAE Formula Student team [37] .....                                              | 35 |
| Figure 14: A diagram of a roller based SLM machine [38].....                                                                          | 36 |
| Figure 15: ORLAS CREATOR SLM machine [54].....                                                                                        | 42 |
| Figure 16: Schematic of the chamber of the ORLAS CREATOR SLM machine .....                                                            | 42 |
| Figure 17: Hardness and ultimate tensile strength values obtained in wrought H13 after tempering at different temperatures [50] ..... | 44 |
| Figure 18: Optical micrograph showing martensite, retained austenite, and carbides in as quenched H13 (quenched at 1050°C) [50].....  | 44 |

|                                                                                                                                                                                                                                                                                                                         |    |
|-------------------------------------------------------------------------------------------------------------------------------------------------------------------------------------------------------------------------------------------------------------------------------------------------------------------------|----|
| Figure 19: Higher hardened depth with increased laser energy density in laser melted H13 tool steel [52] .....                                                                                                                                                                                                          | 45 |
| Figure 20: Melted and hardened layer depth as a function of laser energy density in laser melted H13 tool steel [52].....                                                                                                                                                                                               | 45 |
| Figure 21: SEM micrographs from H13 showing (a) the melted layer and hardened layers after laser surface treatment, (b) hardened layer and heat affected layer, and (c) the base material before laser treatment [52].....                                                                                              | 46 |
| Figure 22: TEM micrographs and corresponding SAD patterns revealing phases in SLMed H13 tool steel (a) ferrite (b) cementite (c) martensite and (d) austenite [53] .....                                                                                                                                                | 47 |
| Figure 23: SEM micrographs obtained from H13 samples after DED and heat treatment at (a) 350°C, (b) 450°C, (c) 550°C, (d) 600°C, and (e) 650°C. All samples were furnace cooled after 2 hours [54].....                                                                                                                 | 48 |
| Figure 24: SEM micrographs of deposited H13 powder on an H13 substrate. Zoomed in images showing the zones in (a) can be found in (b), (c), (d), and (e) with associated hardness values for each zone, (a) substrate and clad, (b) clad zone, (c) inter diffusion zone, (d) heat affected zone and substrate [42]..... | 49 |
| Figure 25: Hardness values for H13 samples manufactured via DED and heat treated at temperatures between 350-650°C [54].....                                                                                                                                                                                            | 50 |
| Figure 26: Comparison between Charpy impact energy for heat treated wrought H13 and H13 samples manufactured via DED and heat treated up to 675°C [54] .....                                                                                                                                                            | 51 |
| Figure 27: SEM micrographs showing laser clad zones and hardness values in H13 tool steel at LED of (a) 120 J/mm <sup>2</sup> , (b) 133 J/mm <sup>2</sup> , and (c) 147 J/mm <sup>2</sup> [42].....                                                                                                                     | 52 |

|                                                                                                                                                                                                                                        |    |
|----------------------------------------------------------------------------------------------------------------------------------------------------------------------------------------------------------------------------------------|----|
| Figure 28: Microhardness by zone for H13 samples of LED values of (1) 120 J/mm <sup>2</sup> , (2) 133 J/mm <sup>2</sup> , and (3) 147 J/mm <sup>2</sup> [54].....                                                                      | 53 |
| Figure 29: SEM images of the laser clad layer after undergoing (a) conventional furnace heat treatment at 550°C and (b) laser assisted surface heating. Hardness values are reported in the upper right corner of each image [48]..... | 54 |
| Figure 30: Malvern Mastersizer3000E particle size distribution analyzer .....                                                                                                                                                          | 56 |
| Figure 31: Hall Flowmeter funnel used for apparent density data collection.....                                                                                                                                                        | 57 |
| Figure 32: Metal powder filled and overflowing the collection cup .....                                                                                                                                                                | 58 |
| Figure 33: Leveled H13 powder in the collection cup.....                                                                                                                                                                               | 58 |
| Figure 34: Tap density experimental setup using the Quantachrome Autotap used here.....                                                                                                                                                | 59 |
| Figure 35: Rapid Temp Furnace by CM Inc. used for homogenizing and heat treatment.....                                                                                                                                                 | 60 |
| Figure 36: SLMed specimen with orientation where the Z-axis of the machine points upward through the cylinder. The ring at the bottom provides additional support during the SLM process.....                                          | 61 |
| Figure 37: SLM process of H13 in an ORLAS CREATOR.....                                                                                                                                                                                 | 62 |
| Figure 38: SLM processing parameters matrix specimens after printing showing specimens and support structure.....                                                                                                                      | 62 |
| Figure 39: SLMed specimens after build plate and support structure removal.....                                                                                                                                                        | 63 |
| Figure 40: Ohaus Pioneer Archimedes density measurement kit.....                                                                                                                                                                       | 64 |
| Figure 41: Pace Technologies PICO155P precision cutting saw for cross sectioning the specimens. ....                                                                                                                                   | 65 |
| Figure 42: TP-7001B Mounting Press by Pace Technologies .....                                                                                                                                                                          | 66 |
| Figure 43: Mounted SLMed specimen ready for metallography .....                                                                                                                                                                        | 66 |

|                                                                                                                                                                                             |    |
|---------------------------------------------------------------------------------------------------------------------------------------------------------------------------------------------|----|
| Figure 44: NANO-2000T Grinder-Polisher by Pace Technologies used for grinding/polishing mounted samples.....                                                                                | 67 |
| Figure 45: Zeiss Axiotron optical microscope .....                                                                                                                                          | 68 |
| Figure 46: Etching setup beneath the fume hood .....                                                                                                                                        | 69 |
| Figure 47: LECO LM 248AT microhardness tester .....                                                                                                                                         | 70 |
| Figure 48: Sample loaded into the microhardness tester in preparation for testing .....                                                                                                     | 70 |
| Figure 49: Temperature profile used for tempering heat treatment of H13 SLMed and homogenized H13 wrought alloy .....                                                                       | 71 |
| Figure 50: SEM micrograph on H13 tool steel powder gas atomized by Carpenter Technology.                                                                                                    | 72 |
| Figure 51: SEM micrograph obtained at higher magnification showing morphology of the H13 powder.....                                                                                        | 73 |
| Figure 52: Discerned particle outlines using ImageJ of a (a) highly magnified micrograph and a (b) lower magnified micrograph.....                                                          | 74 |
| Figure 53: Particle size distribution histogram for all measurements of the H13 powder. X-axis is powder size in $\mu\text{m}$ on a logarithmic scale.....                                  | 75 |
| Figure 54: Profile of the H13 powder in the graduated cylinder upon conclusion of tapping.....                                                                                              | 76 |
| Figure 55: Optical micrograph obtained from as-polished surface of SLMed sample at (a) VED of $25.3 \text{ J/mm}^3$ or sample 1 and (b) VED of $38.0 \text{ J/mm}^3$ or sample 4.....       | 80 |
| Figure 56: Optical micrograph obtained from as-polished surfaces of SLMed samples with (a) VED of $110.6 \text{ J/mm}^3$ (sample 10) and (b) VED of $760.0 \text{ J/mm}^3$ (sample 18)..... | 81 |
| Figure 57: Optical micrographs obtained from as-polished surfaces of homogenized, wrought H13 tool steel samples .....                                                                      | 82 |

|                                                                                                                                                                                                                                                                                                                       |    |
|-----------------------------------------------------------------------------------------------------------------------------------------------------------------------------------------------------------------------------------------------------------------------------------------------------------------------|----|
| Figure 58: Optical micrograph of austenitized and water quenched H13 wrought alloy etched with 2% Nital solution .....                                                                                                                                                                                                | 83 |
| Figure 59: Optical micrograph of SLMed H13 (Sample 18 with VED of 760.0 J/mm <sup>3</sup> and etched with 2% Nital solution) .....                                                                                                                                                                                    | 83 |
| Figure 60: Optical micrographs of tempered H13 tool steel etches with 2 Vol.% Nital solution: (a) wrought and tempered at 500°C, (b) SLMed and tempered at 500°C, (c) wrought and tempered at 550°C, (d) SLMed and tempered at 550°C, (e) wrought and tempered at 600°C and (f) SLMed and tempered at 600°C (e) ..... | 86 |
| Figure 61: Five single-track SLM prints of 316L stainless steel with the same VED value (242 J/mm <sup>3</sup> ). Laser power and scanning speed are shown increasing from the top the bottom of the five images [40] .....                                                                                           | 88 |
| Figure 62: Microhardness data for wrought and SLMed samples at are shown at as-received, as-printed/austenitized and water quenched, 550, 600, and 650°C.....                                                                                                                                                         | 89 |

List of Tables

Table 1: A comparison between commercially available machines on the current market. Laser power, layer thickness, and build volume are compared with these machines [19,34,35,39,43–45] ..... 41

Table 2: ASTM H13 elemental composition [47] ..... 43

Table 3: Chemical Composition of Carpenter H13 Powder (wt.%) ..... 55

Table 4: Elemental Analysis of Wrought H13 [59] ..... 59

Table 5: H13 Printing Parameters Matrix (the numbers in parenthesis are sample numbers) ..... 61

Table 6: SLMed processing parameters samples prepared for metallography ..... 65

Table 7: Apparent Density Data and Calculations ..... 76

Table 8: Archimedes Density of Wrought H13 ..... 77

Table 9: Archimedes Density of SLM Processing Parameters Matrix (different power, scanning speed, and VED) ..... 78

Table 10: Archimedes Density of Heat Treated Samples ..... 79

Table 11: Archimedes Density of Heat Treated Samples ..... 79

Table 12: Microhardness data for the printing parameters matrix ..... 87

Table 13: Microhardness data of the wrought H13 ..... 88

Table 14: Microhardness data of heat treated wrought and SLMed samples at 550, 600, and 650°C ..... 89

## 1 Introduction

Additive manufacturing (AM) is an emerging and quickly growing field disrupting current manufacturing methods. New design opportunities have presented themselves due to the increased demand for design freedom and reduced material waste caused by machining. The field of tooling, plastic injection mold manufacturing and design in particular, has the potential to benefit from rapid tooling (prototyping), design complexity and conformal cooling channels insertion capabilities offered by AM.

The type of AM explored in this study was selective laser melting (SLM), a particular process within the powder bed fusion methodology of AM. In SLM component geometry is generated by melting powder layer by layer with a high energy laser beam. In this study H13 tool steel powder was examined in the SLM process due to its excellent combination of ductility, hardness, and thermal fatigue resistance making it an ideal candidate for molding and rapid tooling applications.

The objective of this study was to identify the role of SLM processing parameters (shown in the form of volumetric energy density) on structure and properties of H13 tool steel components. Gas atomized H13 tool steel powder was procured from Carpenter Technologies. Powder was characterized for density, particle size, morphology and size distribution. SLM processing parameters were optimized to achieve high relevant density and low porosity. Microstructure and mechanical property of wrought H13 tool steel and SLMed H13 tool steel were investigated after SLM and tempering heat treatment. Tempering was conducted at three different temperatures with the intent of achieving a balance between ductility and hardness.

The ultimate goal of this study was to evaluate the SLM process as an alternative additive manufacturing route to build H13 tool steel components that have similar or superior

microstructure and mechanical property than conventionally manufactured (wrought) H13 tool steel. Mechanical properties of SLMed and tempered H13 tool steel were measured to be higher than those of tempered wrought H13 tool steel.

## 2 Literature Review

Several areas of study and processes were explored in the research study. Key areas that will be covered to provide reference include plastic injection molding, types of additive manufacturing, selective laser melting, and H13 tool steel.

### 2.1 Plastic Injection Molding

Injection molding is a manufacturing process that has been around since 1872 when the Hyatt brothers patented the first injection molding machine [1]. The first injection molding machines were made for plastics, but other injection molded materials followed including metals and ceramics [1,2]. The plastic injection molding (PIM) process and related tooling will be discussed in detail below.

#### 2.1.1 Plastic Injection Molding Process

There are two main kinds of PIM machines, piston injection models and the most commonly used type, reciprocating screw variants. Both machines follow similar processes outlined as follows. The PIM process has five main steps: pellets enter the barrel, pellets melt in the heated length of the barrel, either a piston or screw mechanism inject the molten plastic into the mold cavity, the plastic is allowed to cool and solidify in the mold, and the mold is opened while ejector pins push the formed part out of the mold [1,3].

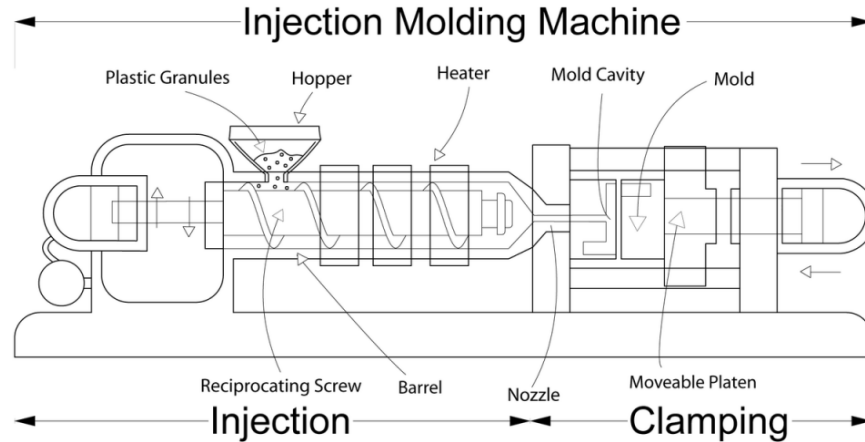


Figure 1: A diagram of a typical reciprocating screw injection molding machine [4]

### 2.1.2 Injection Molding Tooling Features

The most critical piece of the injection molding process is the mold itself. The resulting part has dimensions within tight tolerances if the mold is made correctly, however, as time goes on and the mold starts to deform more post processing is required [1,4]. As the mold continues to deform issues arise because the part duplicates the cavity formed by the mold [5]. There are many features present in an injection mold such as cooling channels for coolant to flow through, and the injection and ejection pins in the tool that include the dimensional properties of each side [5]. These features, their importance, and the manufacturing process used to make the molds will also be investigated.

#### 2.1.2.1 Two-Sided

After the part has solidified in the mold, the part must be removed. In order to do this, molds are typically made with two sides that can be pulled apart allowing the part to drop out. During injection, the clamping force holding the two halves together is of great importance for quality purposes [3]. Chen *et al.* [6] found that mold separation is directly related to the quality of the injection molded part. They found that the mold momentarily separates on the order of microns

when the mold reaches a point of maximum pressure. It is essential to have proper clamping force that limits mold separation while avoiding damage to the sealing faces of the tooling is essential. Therefore, proper machining is required in order to create a smooth sealing faces on each half of the injection molding tooling.

### 2.1.2.2 Cooling Channels

Injection molding is a cyclic process for creating plastic parts rapidly and in large volumes. The faster and more efficiently a molder can make a part, the more revenue the company will have on margin when selling to an original equipment manufacturer (OEM) [7]. One way for molders to increase production is to reduce cycle time. As can be seen in Figure 2, the slowest part of the injection molding process is the cooling time for the part to solidify in the mold.

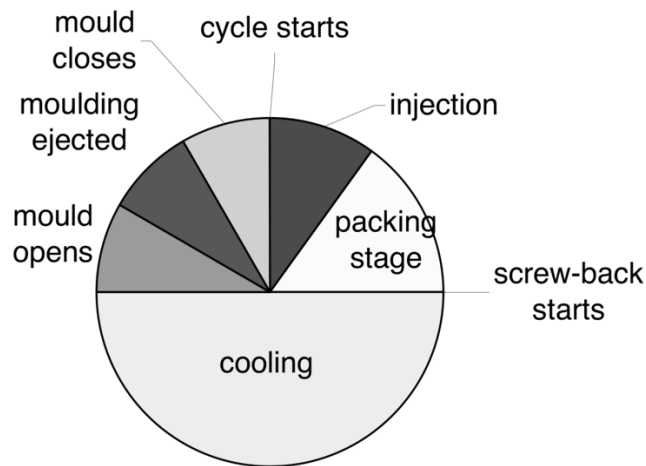


Figure 2: A pie chart showing typical percentages of time spent for each portion of the injection molding process [1]

Cooling the pressurized, molten plastic in the mold is done by running a coolant fluid through cooling channels cut into the mold. By flowing a cool fluid through the channels, the heat is transferred from the plastic, through the mold, to the fluid [3]. Uniform cooling is important for part quality and appearance as well as decreasing cycle time [8]. The more uniform the cooling, the lower the residual stresses present in the part are as well [1]. Conformal cooling channels can

be used to facilitate even cooling of the molded parts by retaining constant offsets to the tooling surface [9].

For the most part, subtractive manufacturing processes are limited by straight cooling channels that vary in distance to the wall of the mold interior. An example of straight, drilled cooling channels can be seen in Figure 3.

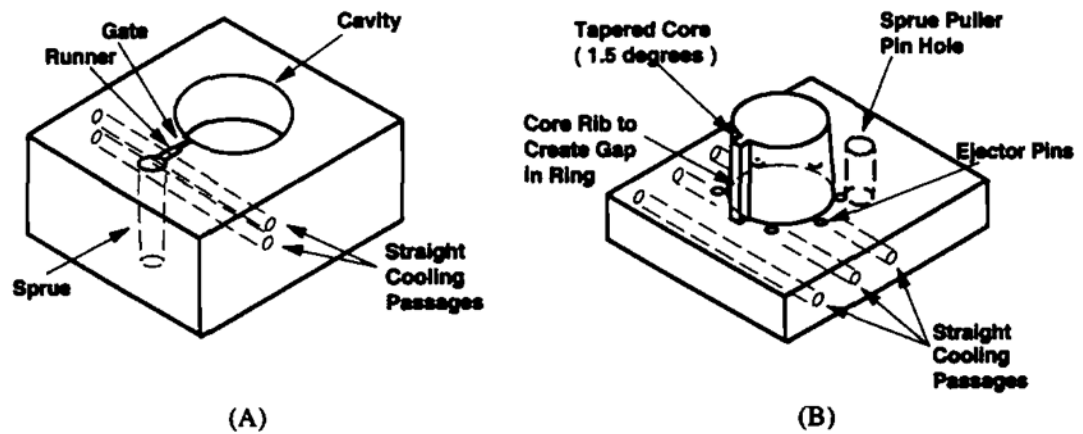


Figure 3: Straight cooling channels presented in both sides of an injection molding tool [10]

Additive manufacturing (AM), commonly referred to as 3D printing, has been used in the past to create conformal cooling channels for injection molds. Sachs *et al.* [9] provided a procedure for creating AM injection molds with conformal cooling channels that positively affect the cooling uniformity of parts and resulted in increased dimensional stability and accuracy of the part. They also found that conformal cooling channels eliminated the transient behavior of the surface temperature of the mold typically found in molds with straight drilled cooling channels. An injection molding tool with conformal cooling channels is presented in Figure 4.

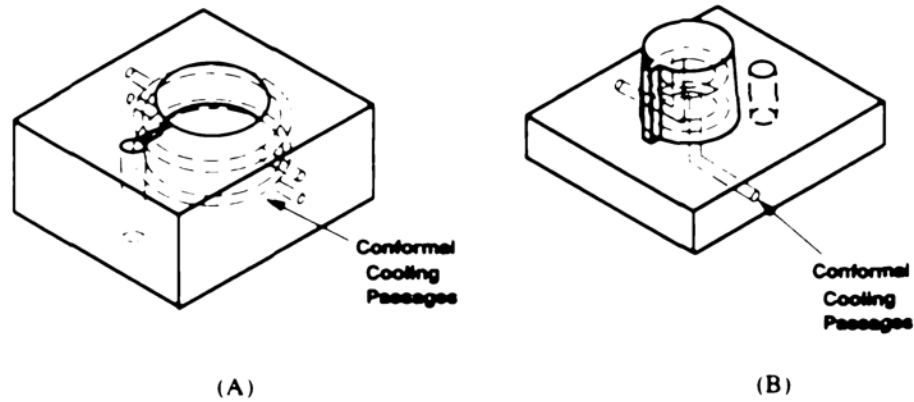


Figure 4: Conformal cooling channels presented in both sides of an injection molding tool [10]

### 2.1.2.3 Injection Gates and Ejection Pins

The injection gate in an injection molding tool is the point at which the molten plastic enters the mold cavity. Molds are usually designed so that when the mold is separated, the excess plastic runner created by the gate is automatically trimmed [10]. This eliminates a secondary operation to remove the runner, ultimately creating savings to the molder which trickle up to the customer.

Ejection pins are used on the side of the mold which retracts in order to push the resulting plastic parts out of the mold. Small deformations on the surface of part are often a result of the ejection pins [11]. Therefore, ejection pins should not be placed on the critical surfaces that must be free of imperfections. To save time during the part removal process the ejector pins are usually extended while the mold is still being separated so that the mold can be closed and injected again quickly.

### 2.1.3 Tooling Production

The design and cost of an injection molding tool depends on tool manufacturing. Ribeiro *et al.* [12] incorporated the incurred costs of injection molding tooling design and manufacturing

into a product's life cycle cost. Factors such as reliability, material consumption, and down time have a significant role on tool's design and manufacturing process.

Another factor in tooling production is the method of manufacturing the mold. There are currently two manufacturing methods; conventional (subtractive machining of a solid block) and hybrid manufacturing, which is a combination of additive and subtractive manufacturing. These two methods will be discussed in the following sections.

#### 2.1.3.1 Conventional Tooling

The conventional tooling process entails subtractive methodology. Typically a solid block of pre-hardened tool steel is cut and shaped with machinery into the desired mold [4]. Some common manufacturing processes involved in conventional tooling include electric discharge machining (EDM) and computed numerical control (CNC) milling, but various other specialty techniques are used as well [13]. Five or three axis CNC mills are commonplace in the milling process while wire and sinker methods are used for EDM machining. Klink *et al.* [14] describe dimensional tolerances and surface roughness as common indicators used to determine mold quality, but also use surface integrity as an additional gauge. Surface integrity is a combination of topographical and surface characteristics that include roughness, residual stresses, hardness, and deformation [15].

#### 2.1.3.2 Limitations of Subtractive Manufacturing

Klink *et al.* [14] found that EDM and milling resulted in excellent dimensional accuracy, but poor surface integrity. In order to achieve high levels of surface integrity, slower, more specialized techniques like laser finishing must be utilized. A mold with poor surface integrity can become plastically deformed or even fail due to formations as a result of the machining process. Martínez-Mateo *et al.* [4] studied surface wear due to varying surface hardness values on

traditionally machined molds. The differing hardness values are due to the mold surfaces being different distances from the original pre-hardened block surface. The researchers suggest a post-machining heat treatment process to ensure uniform hardness of the mold surface. This step will result in homogeneous wearing of the mold surface during part production.

An additional drawback to convectional tooling methods is that the resulting geometry is limited by the machining methods. Complex shapes, cavities, and conformal cooling channels are either impossible or difficult to achieve using traditional machining techniques.

### 2.1.3.3 Additive Manufacturing

Additive manufacturing (AM) provides significant key advantages over traditional, subtractive machining processes. Additive processes build parts one layer of material at a time, generally between 10-50 microns in thickness [16]. This allows for increasingly complex designs with small/internal features to be built much easier than in subtractive manufacturing. For example, conformal cooling channels are one example of a complex shape/cavity that can be created using additive techniques that subtractive methods are incapable to replicate [9].

Significant time savings can be achieved when using additive manufacturing by eliminating the CNC machine programming step in traditional tooling production. CAD models can be realized directly into most 3D printer software without the need for manually deciding tooling paths. Once processing parameters for a given material powder are fine-tuned, they can be used to print virtually any part with minimum delay from design to printing [13].

However, AM is not without drawbacks. Because it is a layer by layer process, increasing accuracy requires reducing the layer thickness. This results in more layers which can increase manufacturing time by decreasing the deposition rate. This is most costly in slow processes such

as selective laser melting (SLM) which can only fabricate 5-20 cubic centimeters of metal/hour [16].

Residual stresses present in printed parts are difficult to predict and overcome and can cause part distortion and cracking. Mukherjee *et al.* [17] investigated residual stresses in 3D printed parts and found that reducing the layer thickness was a valid method for reducing residual stresses but could not totally eliminate the stress.

A final limitation of AM is the part size that is possible to produce. Some techniques such as direct energy deposition (DED) and electron beam melting (EBM) are capable of producing very large (900 x 1500 x 900 mm) components at the cost of reduced accuracy through increased layer thickness [18]. On the other hand, the largest SLM machine on the market currently is the X Line 2000R by Concept Laser which only has a build volume of 800 x 400 x 500 mm [19]. This size envelope is capable of creating molds for small, everyday items, but for larger automotive and aerospace applications the envelope of the X Line 2000R is not large enough yet.

## 2.2 Types of Additive Manufacturing (AM)

There are many types of additive manufacturing readily available. Each method has its own distinctive characteristics that makes it unique in style. They all have their advantages and disadvantages and therefore they must all be considered whenever a new application is considered. A brief overview of the technologies will be discussed below.

### 2.2.1 Material Extrusion

Material extrusion is a wire fed-method of AM. A wire of material is fed into a heated nozzle that melts the material as it passes through which creates a small bead of molten build material [20]. The bead of molten material is pushed out by the material behind it and deposited onto the layer below or the build platform initially. The topmost layer being extruded creates a

cold weld with the layer below and the two bond together. As with all additive manufacturing processes, this process continues layer by layer until the part is complete. This process is possible with both metals and plastics, being extremely popular with the latter option. With plastics, extrusion additive manufacturing is commonly referred to as either fused filament fabrication (FFF) or the trade name, fused deposition modeling (FDM).

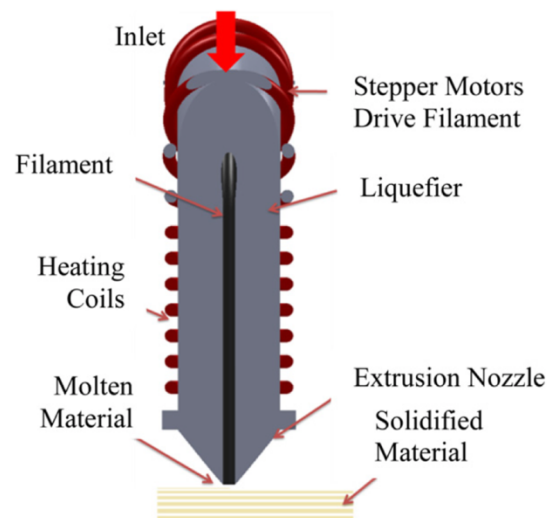


Figure 5: Schematic of a FFF machine nozzle [21]

For high precision FFF processes, the work chamber is typically enclosed and held at a temperature that is slightly lower than the melting temperature of the material being printed [20]. FFF machines also come with chambers that are open to the atmosphere, and typically cost less while sacrificing accuracy.

Metal deposition manufacturing is still underdevelopment, but there are a few ways that it is currently being done. The first has been coined FDMet by Wu *et al.* [22] which stands for fused deposition modelling of metals. The FDMet process consists of wire that is a mix of metal powder and binder being deposited to form a part, a binder removal process, and sintering. This process

shows promise as a lower cost, metal printing process; however further work needs to go into developing process parameters and predicting part shrinkage.

Desktop Metals currently has a machine, the “Studio”, that uses the FDMet process to produce parts on a small scale [23]. This process involves the printer that places the binder and metal combination, a debinder that dissolves the primary binder, and a furnace that brings the metal powder up to just below the melting point to allow the powder to sinter and achieve parts between 96 to 99.8% dense [23–25].



Figure 6: Desktop Metal Studio+ printer [26]



Figure 7: A worm gear printed using Desktop Metal's Studio series of additive manufacturing equipment [27]

Another method of metal extrusion utilizes alloys with low melting temperatures to eliminate the need for binder. Mireles *et al.* [21] used a number of different alloys typically used as soldering material to successfully print 3D parts using the FFF process.

### 2.2.2 Direct Energy Deposition

In direct energy deposition (DED) material can be delivered in wire form, but greater accuracy is accomplished utilizing metal powder due to the small particle size and more concentrated melt pool. The DED process utilizes either a laser beam, electron beam, or pulse arc as the heat source to melt the feedstock, which is then deposited onto the layer or part below [26].

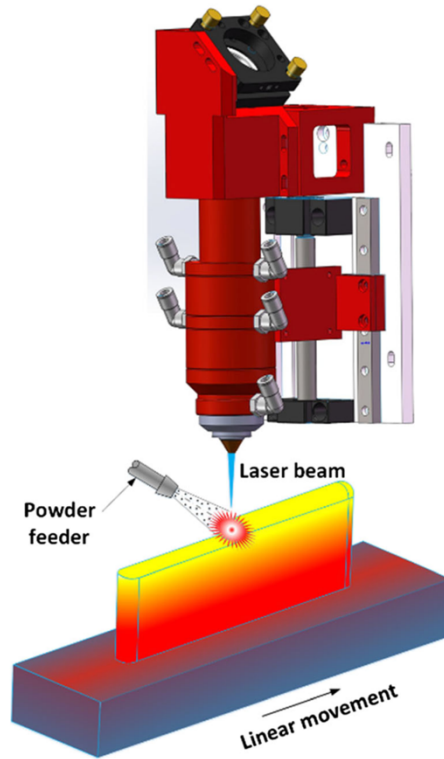


Figure 8: DED machine using a powder feeding system [29]

One of the industry leading vendors of DED technology is Optomec and their LENS® technology systems. Optomec's LENS® systems utilize a high-power laser, metal powder feed, and processing controls to make three dimensional parts [18]. LENS® systems operate within Argon purged environments to limit oxygen and moisture levels below 10 parts per million [18].



Figure 9: The Optomec LENS® 450 system [31]

DED is utilized for both additive manufacturing of low production parts and repairing existing parts manufactured via conventional methods [27]. Repairs are done by taking a part with damage such as cracking or surface cavities and depositing new (repairing) layers using the same alloy with the DED process. Zhang *et al.* [28] found that the characteristics of the substrate such as ultimate tensile strength (UTS) and hardness can be improved by using a repair alloy with higher values. Repairing with DED is important to those industry (e.g. marine applications, turbine blades) where repairing damaged parts is preferred (in terms of lower cost, time, and environmental impact) over creating new parts.

A case study of the repair process was conducted by Wilson *et al.* [29] where they used utilized the DED process to repair the turbine blades made from Nistelle 625 superalloy. In order to make the repairs, a semi-automated geometric algorithm was used to program the DED machine. They found that their mean accuracy was within 0.030 mm of the original blade and their physical testing showed comparable values to other forms of the Nistelle 625 superalloy. In addition to the success of their physical repairs, a life cycle assessment was performed and the repairs showed a 45% improvement in carbon footprint in comparison to the creation of a new blade.

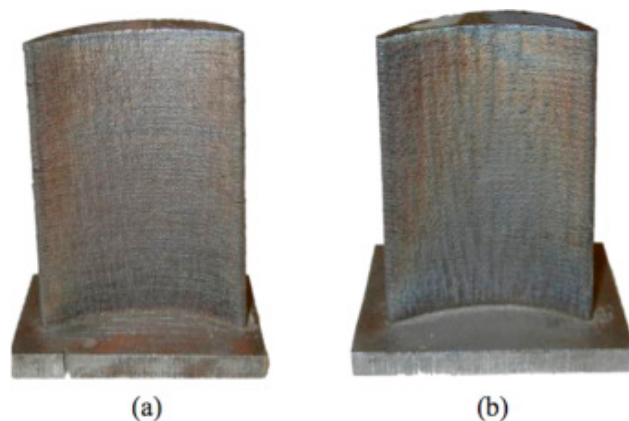


Figure 10: DED used to repair a turbine blade where the (a) undamaged part and (b) the repaired part are presented [29]

### 2.2.3 Powder Bed Fusion

Powder bed fusion (PBF) is an additive manufacturing technique that follows the repetitive process of spreading thin layers of metal powder, then melting the powder using either a laser beam or an electron beam. Laser beams are the most common, with electron beams making up a smaller portion of the market. Selective laser melting (SLM) is the process that uses laser beams to melt the powder and electron beam melting (EBM) is the process that uses electron beams to melt the powder.

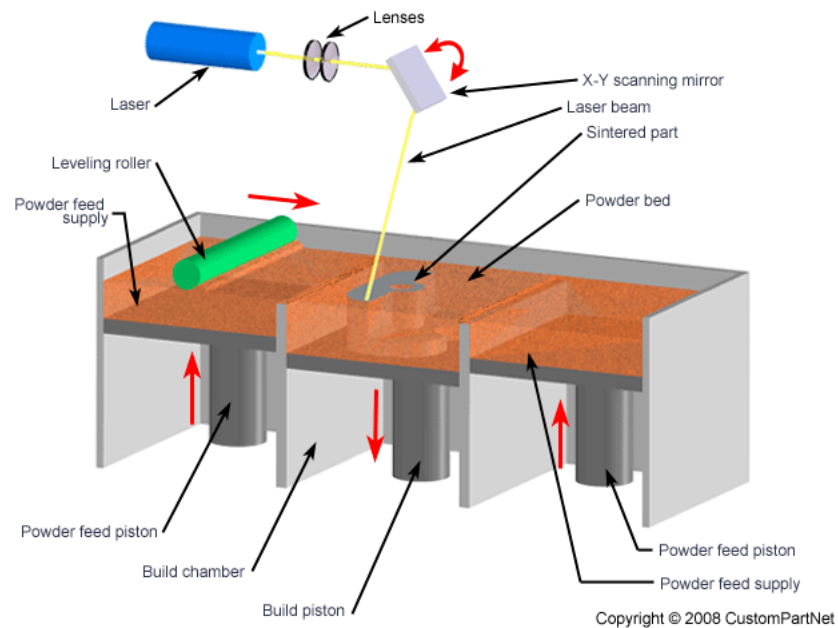


Figure 11: A powder bed fusion machine diagram [34]

The SLM and EBM processes can produce highly accurate parts that have high density and strength when compared to wrought counterparts and require less post processing than other AM processes [30]. In this thesis, the main focus will be on SLM process.

### 2.3 Selective Laser Melting

As stated previously, SLM is a PBF additive manufacturing technique that utilizes a laser beam to melt thin layers of metal powder (usually 50 $\mu$ m). SLM machines are capable of using a

wide variety of materials with the proper printing parameter adjustments. Parts created using SLM can have complex shapes with high accuracy that are unattainable with conventional manufacturing techniques [30]. Examples of SLM manufactured parts can be seen in Figure 12 and Figure 13. Manufacturers of SLM machines currently on the market will be discussed later in Section 2.5.



Figure 12: A titanium alloy aerospace component in an SLM chamber upon completion [36]



Figure 13: SLM manufactured motor cooling hub for an SAE Formula Student team [37]

### 2.3.1 Powder Spreading Techniques

Typically, SLM machines distribute and spread powder with soft blades that push powder across the build platform. Other techniques for distributing powder include dispersing pistons and roller system. A roller system can be seen in Figure 14. In all cases, once a layer has been completed, the build platform drops the thickness of a single layer and another layer of powder is distributed over the top using one of the previously mentioned spreading techniques. Powder is fed into the system with a hopper bin that moves up, bringing more powder into the system, while the build platform moves down [16]. Figure 11 shows an example of this with two feed bins which move up and a single build platform that moves down to allow layers to be placed on top of it.

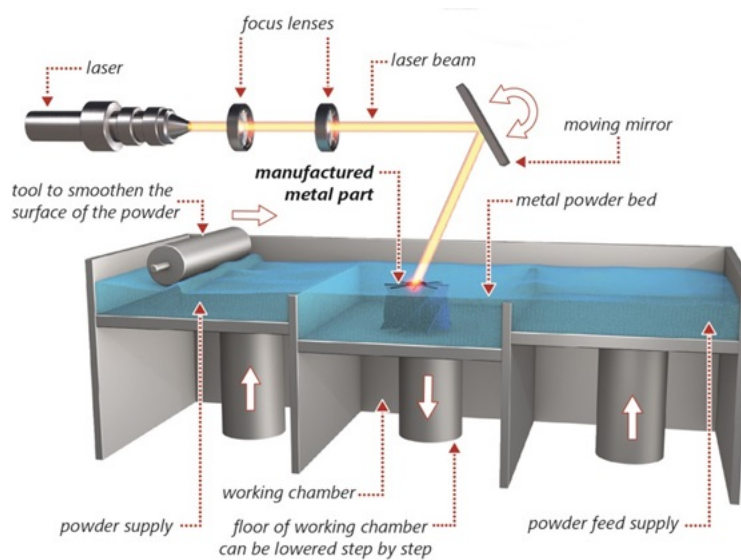


Figure 14: A diagram of a roller based SLM machine [38]

### 2.3.2 Chamber Conditions

The SLM process takes place within a confined chamber with an inert gas atmosphere primarily to prevent oxidation and metal combustion during melting. Oxidation of the material is not ideal because it hinders the melting of the powder and reduces the wetting properties [31]. When thick oxides are present they cannot be completely vaporized which reduces the amount of

metal powder that is melted and thus reduces the stability of the melt pool. Oxidation also leads to increased balling which reduces part quality characteristics such as strength, surface finish, and dimensional accuracy [31]. Two commonly used inert gases in SLM chambers that are readily available include nitrogen and argon.

The importance of the atmospheric pressure was studied by Masmoudi *et al.* [32] using modeling techniques and argon. They found that pressures below 100 mbar contributed to material evaporation due to the reduction in temperature difference between the powder's melting and vaporization points. In contrast, high pressure environments reduced material vaporization and contained the vapor into a smaller volume.

### 2.3.3 Deposition Rate

Deposition rate is a term used in AM to define the amount of material that a machine can manufacture in a given time period. This is typically reported as a value of volume over time such as cubic centimeters per hour, but sometimes is reported as a mass per unit time such as kilograms per hour [19,33]. The deposition rate of a particular machine is entirely dependent on the processing parameters that will be discussed in Section 1.1.5

The depositions rate of an SLM machine varies a lot from machine to machine. The larger machines typically have faster deposition rates to compliment the larger building platforms. A few machines on the higher end of the deposition rate spectrum currently on the market include the Concept Laser X Line 2000R with a deposition rate of 120 cm<sup>3</sup>/h, SLM Solutions' SLM 500 with a rate of 171 cm<sup>3</sup>/h, and Renishaw's RenAM 500Q with a rate of 150 cm<sup>3</sup>/h [19,34,35]. Smaller machines typically have much smaller deposition rates like the Trumpf TruPrint1000 which has a deposition rate of only 2-18 cm<sup>3</sup>/h [36]. However, it should be noted that deposition rate is highly dependent on the parameters the machine is set with as will be discussed in the next section.

## 2.4 SLM Processing Parameters

Processing parameters are different variables that must be optimized during the SLM process. Some significant parameters that will be covered in detail include the laser power, laser scanning speed, layer thickness, and hatch spacing. Definitions of the previously mentioned parameters can be found in Sections 2.4.1, 2.4.2, 2.4.3, and 2.4.6, respectively. The quality of a part, especially density, is sensitive to processing parameters, or the volumetric energy density (VED) provided to the part during SLM manufacturing [31]. VED will be discussed in Section 2.4.4. No single parameter is more important than the rest, they must all be optimized for ideal 3D printing performance.

### 2.4.1 Laser Power

Laser power refers to the power being delivered to the powder through the laser scanning. The strength of the laser can be adjusted to accommodate different materials requiring more or less energy to reach fusion state. Without adjusting other parameters, too much laser power can lead to excessive evaporation and otherwise, too little which results in lack of fusion (LOF) [37].

### 2.4.2 Laser Scanning Speed

Laser scanning speed is the speed of the laser moving along its path. A normal laser scanning speed is typically around 100 mm/s depending on laser power settings [38]. Scanning speed can vary greatly depending on the machine used, getting up to 7000 mm/s on the EOS M 400 [39]. Slower scanning speeds mean that each powder particle is in contact with the beam for a greater time meaning more energy is delivered to each grain if all other settings remain the same. Slower scanning speeds also result in a slower cooling rate [40].

### 2.4.3 Layer Thickness

Layer thickness is a machine parameter that adjusts the height of each layer of powder that is swept over the previous work layer. A very wide range of thicknesses can be used, but to ensure that the melt pool reaches all powder, layers cannot get too thick. Large layer thicknesses result in faster printing by reducing the number of total layers that need to be laid and melted. The minimum layer height is limited by the powder being used. Sufiiarov *et al.* [41] found that parts with smaller layer thicknesses had higher yield strength and ultimate tensile strength values than those with larger layer thicknesses.

### 2.4.4 Volumetric Energy Density

Many defects in SLM manufactured parts can be accounted for by LOF. When there is powder present within a part that has not been fused there has been LOF. An insufficient amount of energy being delivered to the powder by the laser is the dominant reason for LOF [37]. One way to measure the amount of energy being imparted on a part is by utilizing volumetric energy density (VED). VED is calculated using Equation 1 where P is laser power, v is laser scanning speed,  $\sigma$  is hatch spacing, and t is layer thickness [42].

$$VED = \frac{P}{v\sigma t} \left[ \frac{J}{mm^3} \right] \quad (1)$$

From this equation the relationship between laser power, hatch spacing, scanning speed, and layer thickness are related in the production of parts. Adjusting any one setting can alter the VED value. If VED is too low, LOF occurs; if VED is too high, excessive evaporation occurs in the parts. Bertoli *et al.* [40] found that VED is useful, however it does not capture melt pool physics and therefore cannot be solely used to predict printing quality.

#### 2.4.5 Laser Energy Density

Another property very similar to VED that is often used to describe the parameters during laser AM processes is the laser energy density (LED). LED takes into consideration the same parameters as VED but omits the layer thickness. This is particularly useful for describing DED processes that do not have a controlled layer thickness. LED is calculated using Equation 2 where  $P$  is laser power,  $v$  is laser scanning speed, and  $\sigma$  is hatch spacing [42].

$$LED = \frac{P}{v\sigma} \left[ \frac{J}{mm^2} \right] \quad (2)$$

#### 2.4.6 Hatch Spacing

Hatch spacing is the distance between each row the laser beam scans. A hatch spacing that is too large could result in rows of untouched powder that is not melted. Darvish *et al.* [37] found that even established and supported processing parameters for materials result in areas with LOF due to hatch spacing being too large.

### 2.5 Selective Laser Melting Machines

There are many SLM machines on the markets from a number of different suppliers. A handful of offerings are shown in Table 1. Companies represented include SLM Solutions, Renishaw, 3D Systems, Concept Laser, Trumpf, DMG Mori, and EOS.

Table 1: A comparison between commercially available machines on the current market. Laser power, layer thickness, and build volume are compared with these machines [19,34,35,39,43–45]

| Company       | Machine       | Laser Power | Layer Thickness        | Build Volume                         |
|---------------|---------------|-------------|------------------------|--------------------------------------|
| SLM Solutions | SLM 500       | 4x700W      | 20 – 75 $\mu\text{m}$  | 500x280x365 mm                       |
| Renishaw      | RenAM 500Q    | 4x500W      | 20 – 100 $\mu\text{m}$ | 250x250x350 mm                       |
| 3D Systems    | ProX DMP 320  | 500W        | 10 – 100 $\mu\text{m}$ | 275x275x380 mm                       |
| Concept Laser | XLine 2000R   | 2x1000W     | 30 – 150 $\mu\text{m}$ | 800x400x500 mm                       |
| Trumpf        | TruPrint 5000 | 3x500W      | 30 – 150 $\mu\text{m}$ | $\varnothing$ 300 mm x 400 mm height |
| DMG Mori      | LASERTEC 30   | 1000W       | 20 – 100 $\mu\text{m}$ | 300x300x300 mm                       |
| EOS           | M 400         | 1 kW        | 20 – 100 $\mu\text{m}$ | 400x400x400 mm                       |

### 2.5.1 ORLAS Creator

The SLM machine to be used in experimentation for this research project is the ORLAS Creator machine. The Creator is a smaller 3D printing machine more focused on research and precision than high part output like some of the larger machines previously mentioned on the market. Some key features of the Creator machine are a 250W ytterbium fiber laser,  $\varnothing$  100 x 100 mm build chamber, 20 – 100  $\mu\text{m}$  powder layer thickness, and an argon or nitrogen inert atmosphere [46].



Figure 15: ORLAS CREATOR SLM machine [54]

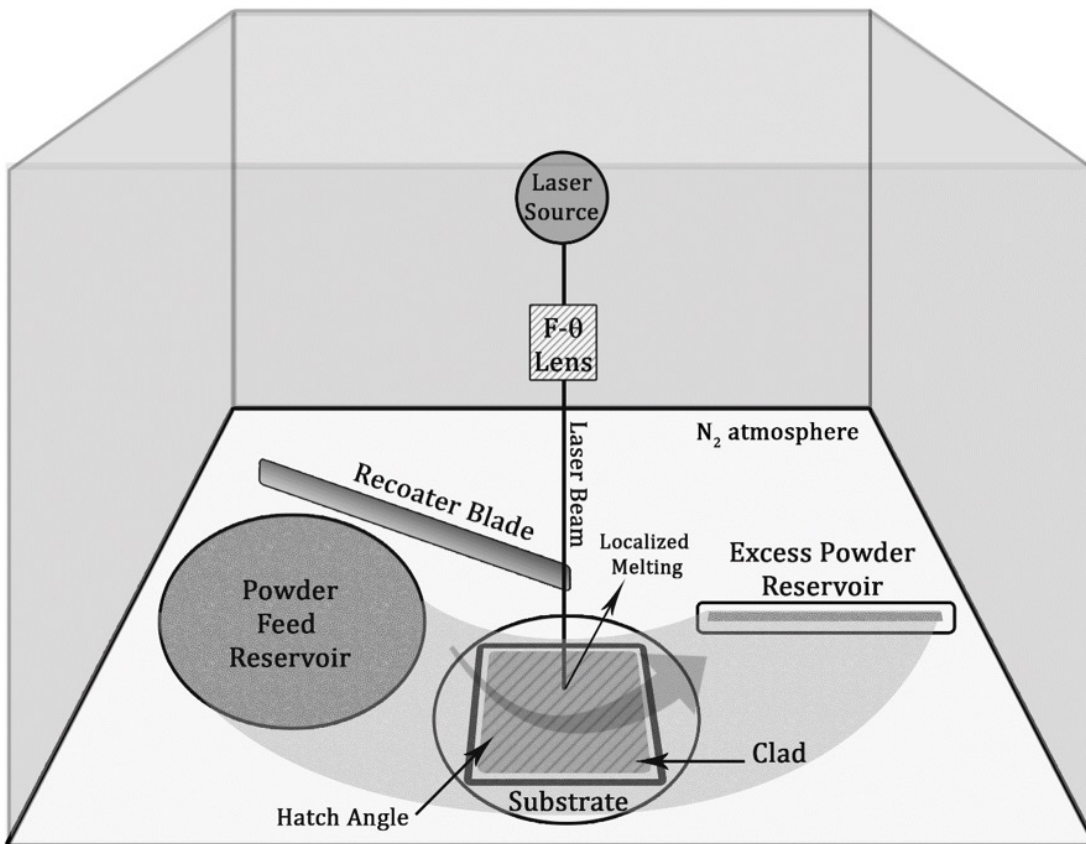


Figure 16: Schematic of the chamber of the ORLAS CREATOR SLM machine

## 2.6 H13 Tool Steel

ASTM H13 tool steel, or just H13, is a hot worked tool steel with relatively low carbon content (0.32 – 0.45 wt%) [47]. H13 is commonly used for die cast molds and plastic injection molds due to good wear resistance while having good toughness and ductility to resist fatigue stresses common in mold usage [48].

### 2.6.1 Wrought Properties of H13

H13 compositions vary slightly by manufacturer, but the ASTM H13 tool steel standard is shown in Table 2. Microstructure is dependent upon the desired phases and how the material is heat treated to achieve those desired phases. Austenite, martensite, ferrite, and carbides ( $\text{Fe}_3\text{C}$ ) are some possible microstructures present within H13, with more than one microstructure typically being represented within a sample [49].

Table 2: ASTM H13 elemental composition [47]

| Element | Fe   | Cr     | Mo     | V      | Mn     | Ni+Cu | Si     | C      | P     | S     |
|---------|------|--------|--------|--------|--------|-------|--------|--------|-------|-------|
| Wt.%    | Bal. | 4.75 – | 1.10 – | 0.80 – | 0.20 – | 0.75  | 0.80 – | 0.32 – | 0.030 | 0.030 |
|         |      | 5.50   | 1.75   | 1.20   | 0.60   | max   | 1.25   | 0.45   | max   | max   |

In an injection mold, high hardness is required and H13 is very receptive to being hardened through heat treatment. A tempered piece of H13 at 552°C results in hardness values in the range of 52 on the Rockwell C hardness scale [47,48]. H13 tool steel has high wear resistance due to the presence of 1 wt% V [48] and its high toughness and ductility along with relatively high hardness. A plot of hardness and tensile strength versus tempering temperature of H13 is shown in Figure 17 [50]. Guanghai *et al.* [50] reported that increase in toughness that coincides with a decrease in hardness, and that excellent strength and toughness was achieved when H13 was tempered at temperatures between 550 – 650°C [50]. The quantity of vanadium in H13 is around one percent

and contributes to its high wear resistance [48]. H13 tool steel also has an excellent polished surface making it a good choice for molds that require high surface finish requirements [51]. Microstructure of H13 after being quenched to form martensite, retained austenite, and carbides is shown in Figure 18 [50].

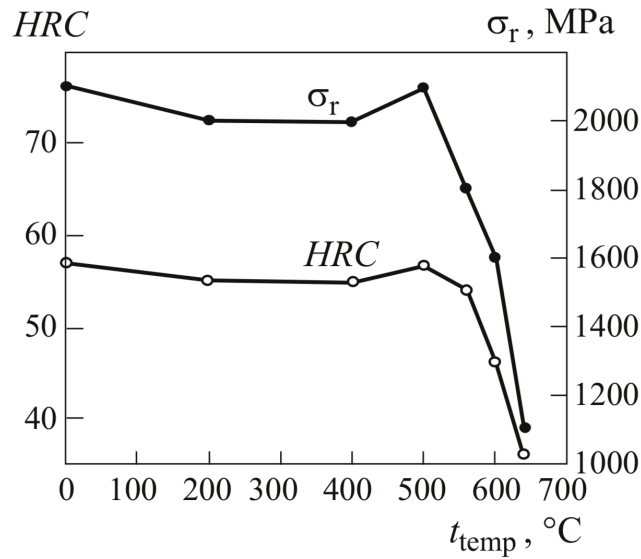


Figure 17: Hardness and ultimate tensile strength values obtained in wrought H13 after tempering at different temperatures [50]

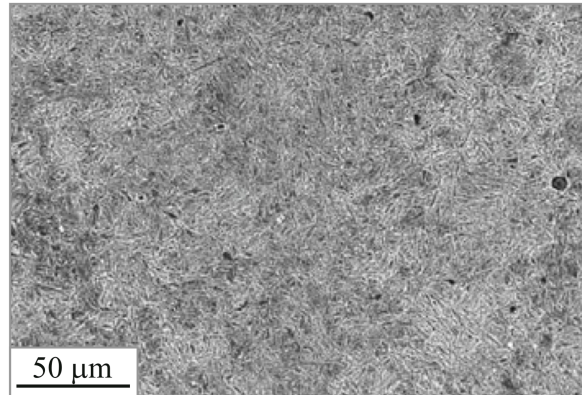


Figure 18: Optical micrograph showing martensite, retained austenite, and carbides in as quenched H13 (quenched at 1050°C) [50]

Chiang *et al.* [52] showed that hardness of H13 steel can be increased by using a laser to melt the surface. The laser energy density (LED) of the laser was found to be directly related to the depth of hardened tool steel as shown in Figure 19 and Figure 20.

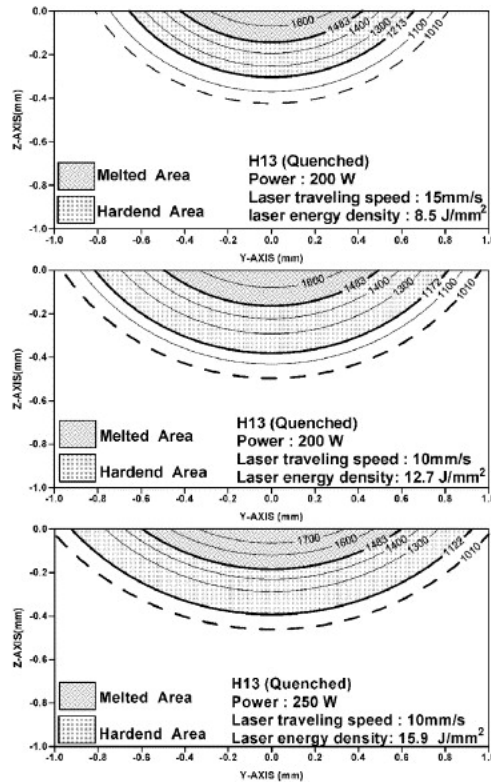


Figure 19: Higher hardened depth with increased laser energy density in laser melted H13 tool steel [52]

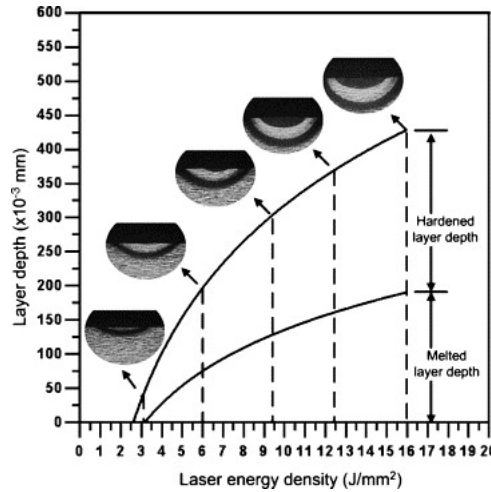


Figure 20: Melted and hardened layer depth as a function of laser energy density in laser melted H13 tool steel [52]

The hardened area consisted of martensite and carbides that precipitated at the grain boundaries. Figure 21a-c show the H13 with hardened areas, the melted area, heat affected layer and the base alloy before undergoing laser treatment, respectively.

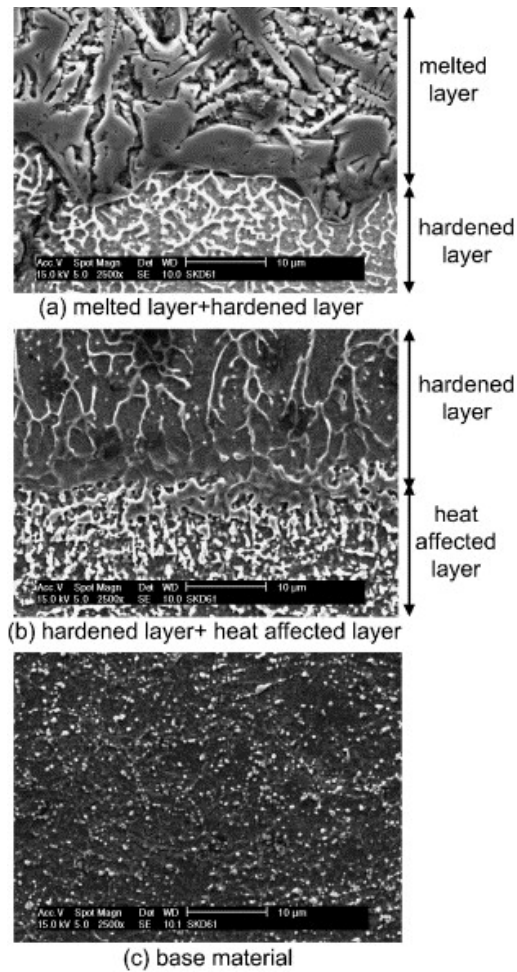


Figure 21: SEM micrographs from H13 showing (a) the melted layer and hardened layers after laser surface treatment, (b) hardened layer and heat affected layer, and (c) the base material before laser treatment [52]

## 2.6.2 Microstructure of Additively Manufactured H13 Tool Steel

Microstructural evolutions in SLMed H13 has been studied by Yan *et al.* [53]. No heat treatment was done to the SLMed samples, and the authors suggest this as a future area of research. Martensite, retained austenite, alpha-ferrite, and cementite precipitates were observed in SLMed H13 as shown in transmission electron microscopy (TEM) micrographs and corresponding selected area diffraction (SAD) patterns presented in Figure 22 [53]. Furthermore, high residual stresses were measured in the specimen just two layers into the SLM process and were likely due to the formation of martensitic phase.

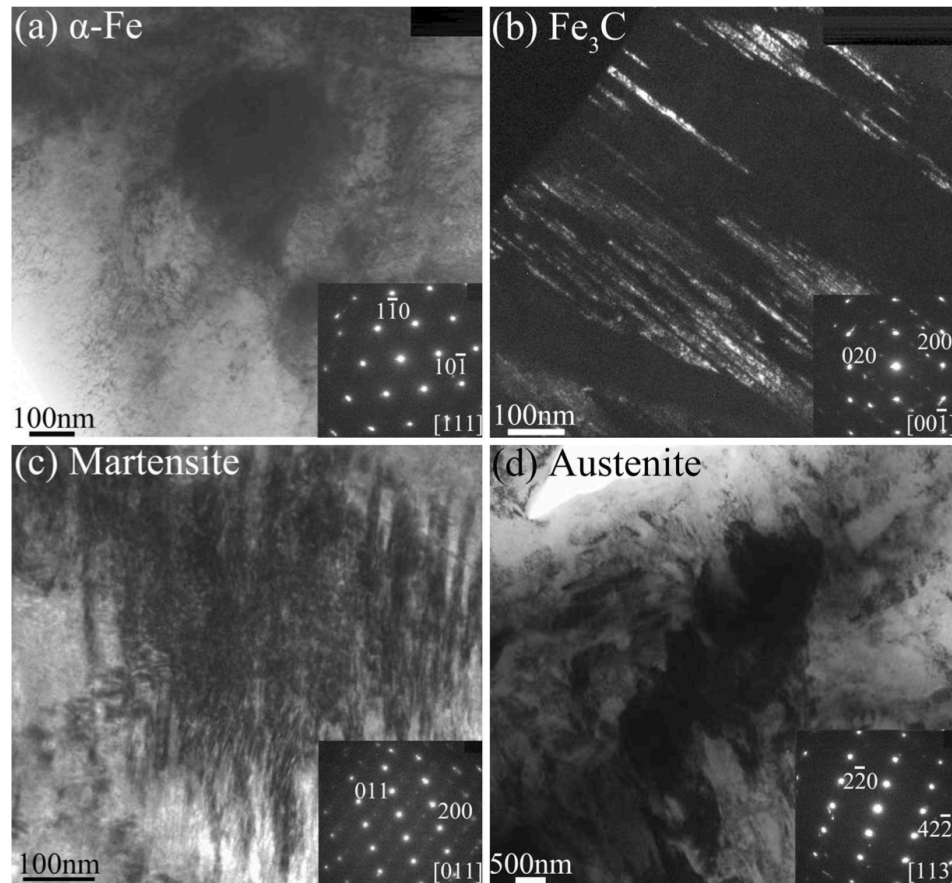


Figure 22: TEM micrographs and corresponding SAD patterns revealing phases in SLMed H13 tool steel (a) ferrite (b) cementite (c) martensite and (d) austenite [53]

Chen *et al.* [54] studied the effect of heat treatment on H13 samples additively manufactured via DED process. As-deposited samples were tempered at temperatures varied from 350, 450, 550, 600, to 650°C for two hours followed by furnace cooling. Microstructure of as-deposited samples contained martensite, fine carbides, and retained austenite. Chen *et al.* [54] attributed the retained austenite to the fast cooling rate during DED process. According to Chen *et al.* [54] rapid cooling rate during the DED process can suppress carbides precipitation and growth, allowing more alloying elements to dissolve in austenite, which reduces the martensite start transformation temperature ( $M_s$ ), thus resulting in retained austenite at room temperature. After

heat treatment, the majority of the retained austenite transforms into tempered martensite and carbides continued to precipitate as shown in Figure 23.

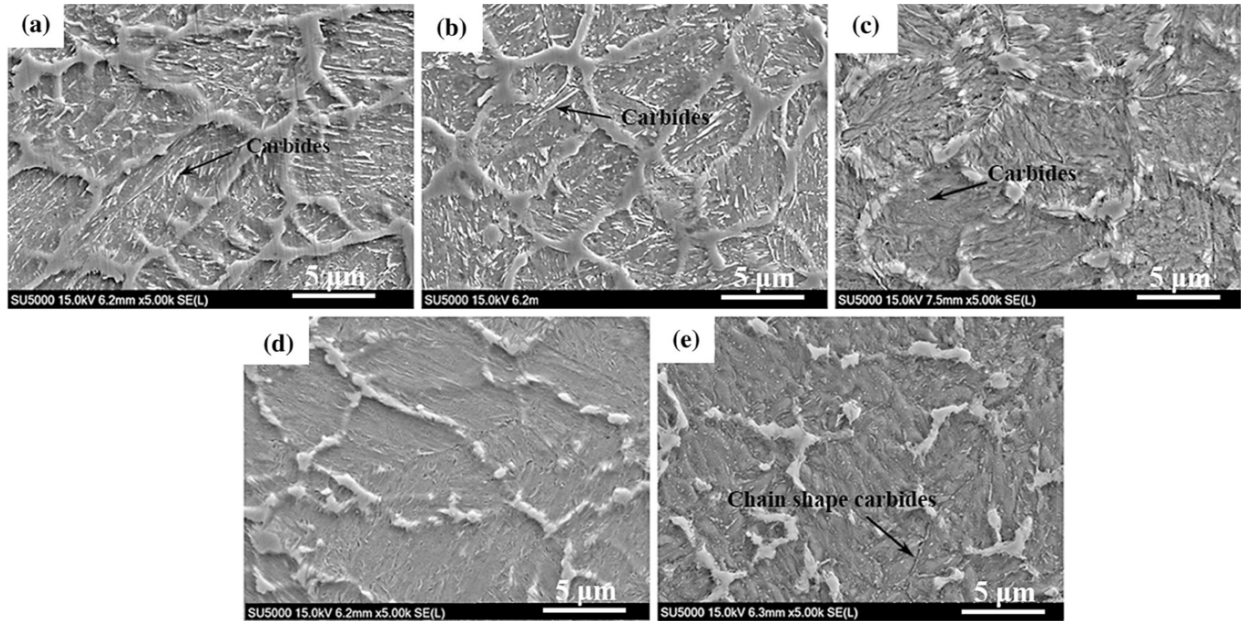


Figure 23: SEM micrographs obtained from H13 samples after DED and heat treatment at (a) 350°C, (b) 450°C, (c) 550°C, (d) 600°C, and (e) 650°C. All samples were furnace cooled after 2 hours [54]

Telasang *et al.* [42] examined the differences between H13 powder deposited onto an H13 substrate via DED process (in need of repair like the process previously mentioned in section 2.2.2). Microstructure was observed to be varied by depth during laser cladding H13. The microstructure of the clad section of the metal showed dendrites with carbides filling the gaps along with martensite and retained austenite [42]. Fine carbides were present as depth increased. In the lower portion of the heat affected zone (HAZ) the microstructure became similar to that of the substrate with the addition of over-tempered martensite leading to decreased hardness. SEM micrographs of each layer is shown in Figure 24.

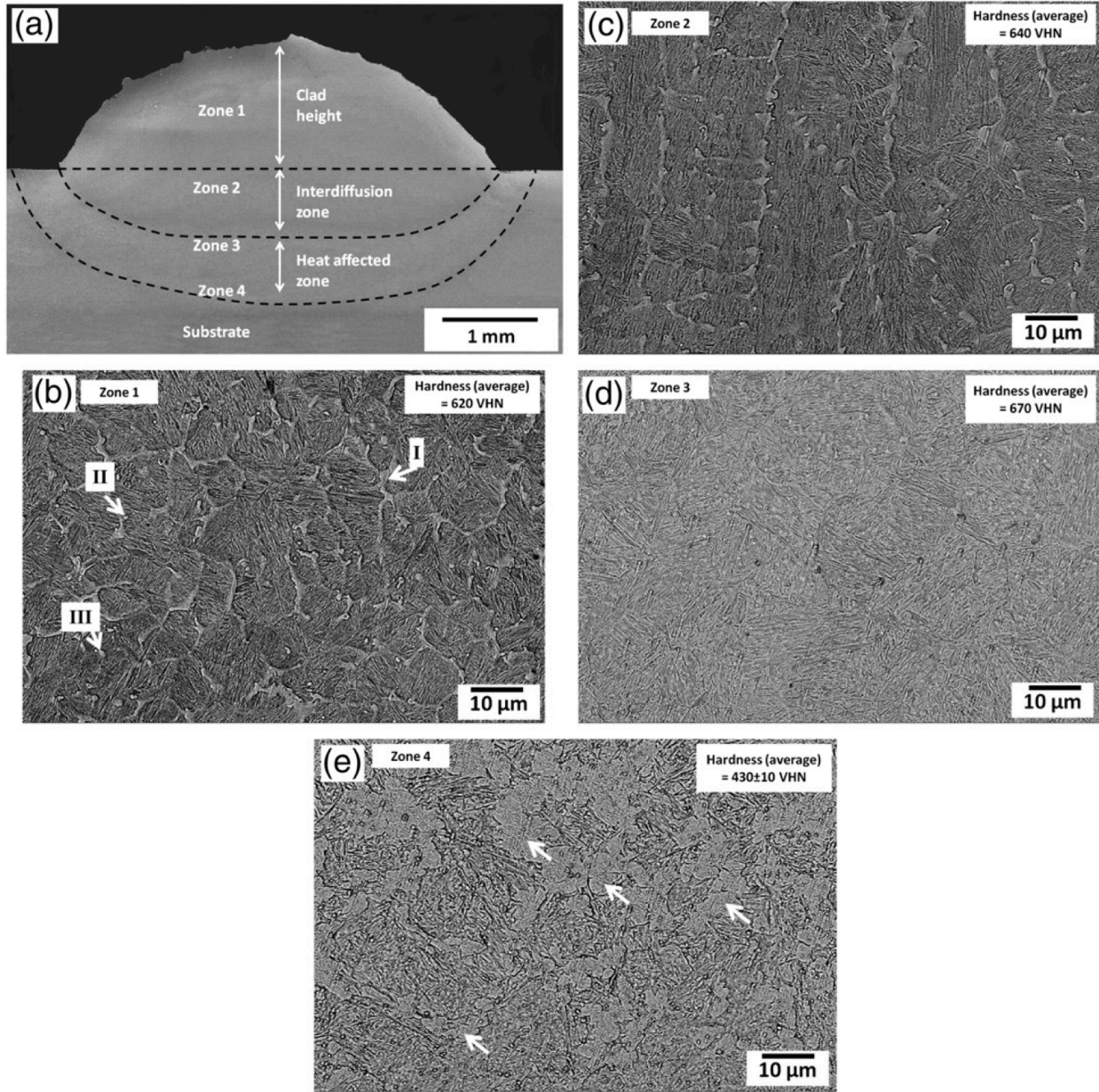


Figure 24: SEM micrographs of deposited H13 powder on an H13 substrate. Zoomed in images showing the zones in (a) can be found in (b), (c), (d), and (e) with associated hardness values for each zone, (a) substrate and clad, (b) clad zone, (c) inter diffusion zone, (d) heat affected zone and substrate [42]

### 2.6.3 Mechanical Properties of Additively Manufactured H13 Tool Steel

Chen *et al.* [54] measured mechanical properties of H13 after DED and heat treatment. Peak hardness occurred in the deposited samples and heat treated at 550°C due to precipitation hardening from the carbides. Hardness values decreased after 550°C due to coarsening of carbides

leading to more ductility and increased toughness. Wrought H13 heat treated at 550°C was compared to H13 manufactured via DED and heat treated at 550°C, and the hardness values were found to be 510 HV and 600 HV, respectively. Hardness variations in wrought H13 and H13 samples manufactured via DED and heat treated at temperatures between 350-650°C are shown in Figure 25.

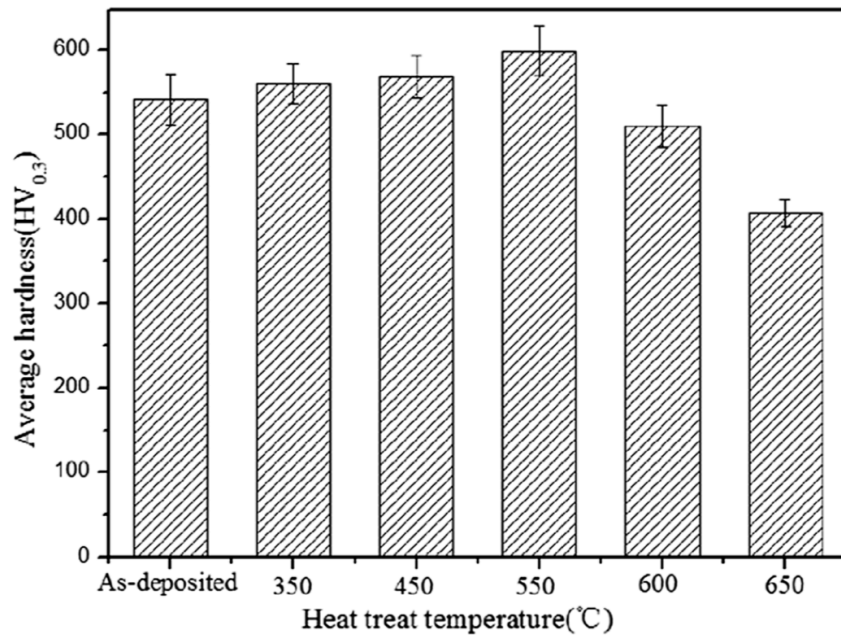


Figure 25: Hardness values for H13 samples manufactured via DED and heat treated at temperatures between 350-650°C [54]

H13 tool steel samples manufactured via DED showed significantly lower Charpy impact energies compared to heat treated wrought H13 as shown in Figure 26.

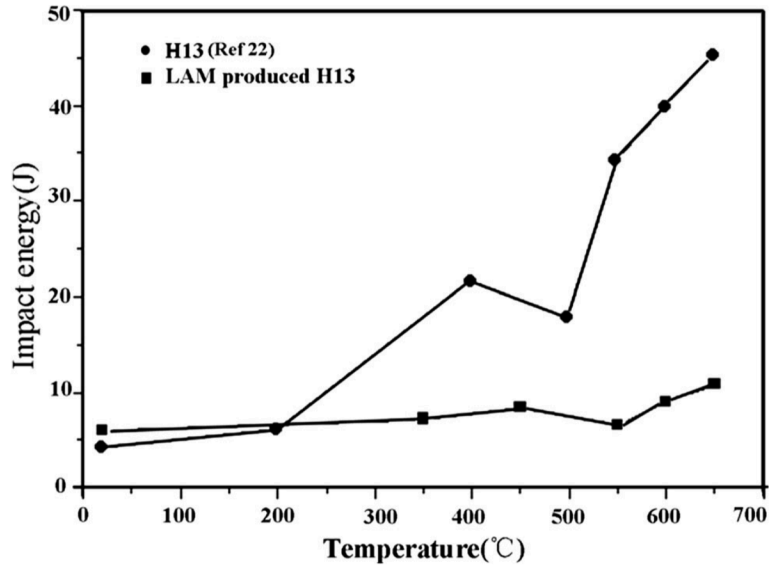


Figure 26: Comparison between Charpy impact energy for heat treated wrought H13 and H13 samples manufactured via DED and heat treated up to 675°C [54]

Telasang *et al.* [42] examined the effects of LED on hardness in the clad zone. According to Telasang *et al.* [42] reduced LED resulted in higher hardness values within the laser clad zone. Microstructure and corresponding hardness values for differing LED values are shown in Figure 27.

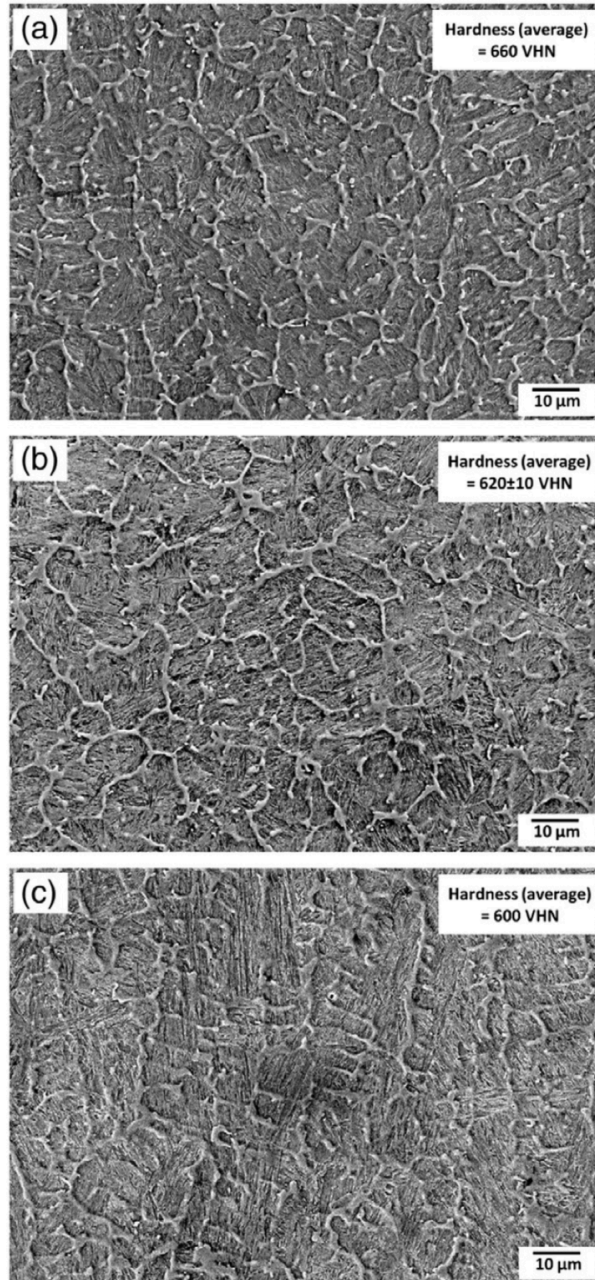


Figure 27: SEM micrographs showing laser clad zones and hardness values in H13 tool steel at LED of (a) 120 J/mm<sup>2</sup>, (b) 133 J/mm<sup>2</sup>, and (c) 147 J/mm<sup>2</sup> [42]

A plot showing the microhardness of the material at varying depths for three separate VED values is shown in Figure 28. Microhardness peaks for all three VED values at the start of the HAZ, with the maximum being approximately 730 HV observed in the 147 J/mm<sup>2</sup> LED sample.

Over tempering is likely the cause for the dip in hardness at the opposite end of the HAZ, with the minimum being approximately 400 HV observed in the 133 J/mm<sup>2</sup> sample.

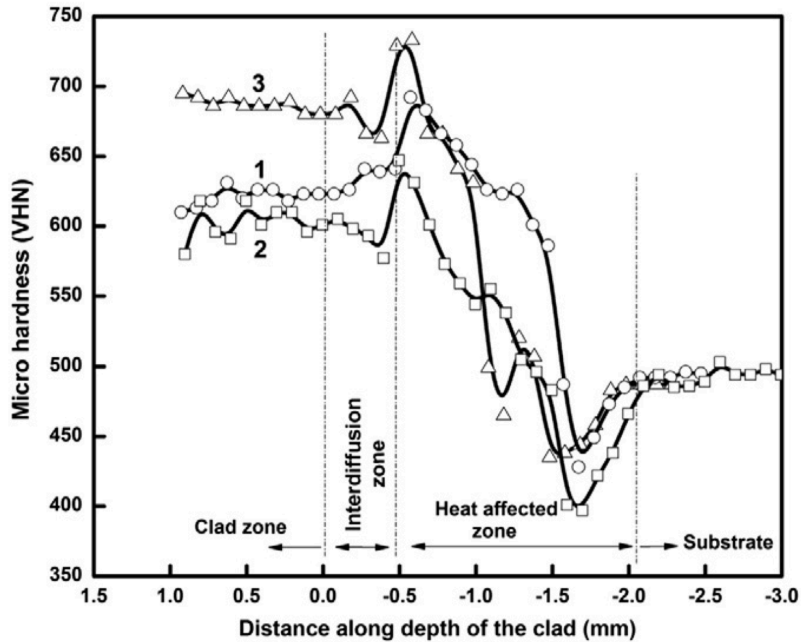


Figure 28: Microhardness by zone for H13 samples of LED values of (1) 120 J/mm<sup>2</sup>, (2) 133 J/mm<sup>2</sup>, and (3) 147 J/mm<sup>2</sup> [54]

Telasang *et al.* [42] compared conventionally heat treated H13 with laser assisted surface heating. Heat treatment was done at 550°C for two hours followed by furnace cooling. The conventionally heat-treated sample showed a 10% increase in carbide precipitates and a decrease in microhardness values from 620 VHN to 590 VHN. Whereas, the laser surface treated sample showed a refined microstructure consisted of new dendrites with martensite, retained austenite, and carbides. The hardness of the laser surface treated sample increased from 620 VHN to 690 VHN.

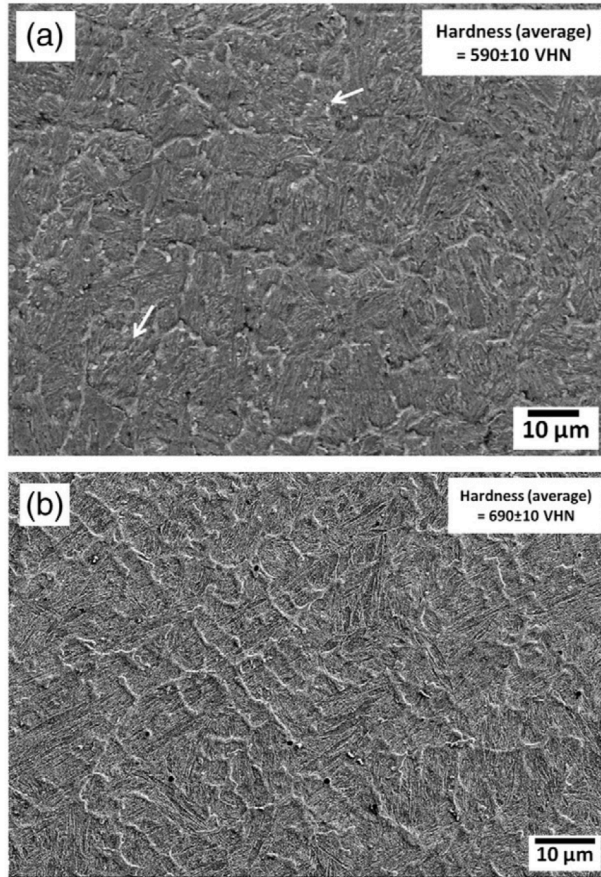


Figure 29: SEM images of the laser clad layer after undergoing (a) conventional furnace heat treatment at 550°C and (b) laser assisted surface heating. Hardness values are reported in the upper right corner of each image [48]

## 2.7 Background Review

The knowledge gained from the literature review allowed for informed decisions to be made regarding the methodology of the research. Valuable information regarding microstructure, mechanical properties, and heat treatment are just a few key pieces of information that shaped the experiment. The information obtained during the literature review and the results of the experiments will be used evaluate the objective of this study, which is to determine whether SLMed H13 tool steel is a valid option for use in plastic injection molds

### 3 Materials and Methods

Procedures to evaluate SLM H13 tool steel samples are as follow; powder density and particle size distribution were examined, SLM processing parameters were developed, and samples were tempered at three different temperatures. Optical microscopy was used to evaluate morphology, porosity and microstructure while microhardness testing was conducted to evaluate mechanical properties.

#### 3.1 H13 Powder Feedstock for SLM Process

Spherical, gas-atomized H13 was procured from Carpenter Technology Corporation. The chemical composition of the powder as specified by the manufacturer is given in Table 3.

Table 3: Chemical Composition of Carpenter H13 Powder (wt.%)

| Element | Fe    | Cr   | Mo   | V    | Mn   | Ni   | Si   | C    | P    | S    | Cu   | N    |
|---------|-------|------|------|------|------|------|------|------|------|------|------|------|
| Wt.%    | 90.05 | 5.16 | 1.43 | 1.03 | 0.42 | 0.20 | 1.06 | 0.42 | 0.02 | 0.01 | 0.07 | 0.03 |

##### 3.1.1 Morphology of H13 Powder

Morphology and particle size of H13 tool steel was identified using a FEI QUANTA 600FEG scanning electron microscope. Powder was prepared for SEM by putting a small piece of carbon tape on an SEM compatible mount. A thin layer of powder was then manually deposited on the carbon tape and extra powder was tapped off.

ImageJ, an image analysis software developed by the National Institute of Health (NIH), allowed for particle size analysis to be conducted using the captured SEM micrographs. In order to accomplish this, thresholding was used on the greyscale pixel values. Pixels with values below a specified value were set to 0 and those with values greater than or equal to that value were set to 255. This resulted in an image exclusively composed of white and black pixels. The software then used the contrasting black and white colors to identify particle boundaries.

### 3.1.2 Particle Size Distribution Analysis

The H13 powder's particle size distribution was analyzed using the Malvern Mastersizer 3000E as shown in Figure 30. This method uses laser diffraction to measure particle size between  $0.1\mu\text{m}$  and  $1000\mu\text{m}$  [55]. The wet method of dispersion was utilized here.



Figure 30: Malvern Mastersizer3000E particle size distribution analyzer

Deionized water (DI water) was used for the method of dispersion. Powder was added to the deionized water supply until a laser obscuration greater than 5% was achieved. A range of stirring speeds between 2200 RPMs and 2750 RPMs was used with the wet dispersion attachment. Additionally, a small concentration of soap was added to the deionized water for some trials to help reduce surface tension trapping smaller particles at the surface of the test beaker containing the water/powder mixture.

### 3.1.3 Density Measurement

Apparent density and tap density of powder were measured as explained in Sections 3.1.3.1 and 3.1.3.2, respectively. Apparent density examines the flowed density of a powder without any additional settling. Tap density provides a settled powder density.

### 3.1.3.1 Apparent Density

The apparent density (AD) of the H13 powder was found using the Hall Flowmeter funnel shown in Figure 31 and following ASTM B212 test procedures [56]. The collection cup had a volume of 25 cubic centimeters.

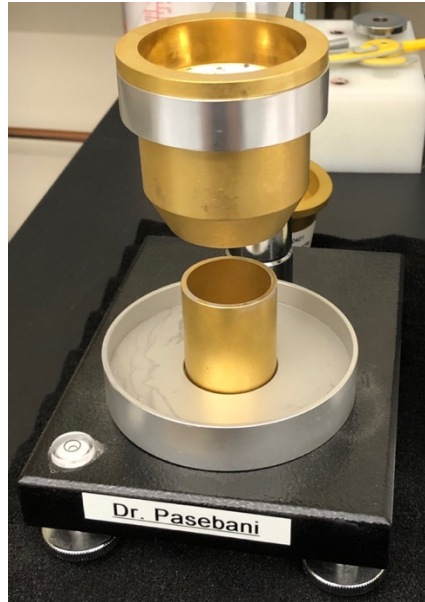


Figure 31: Hall Flowmeter funnel used for apparent density data collection

Powder was flowed into the collection cup until overflowing the cup like shown in Figure 32. Once powder flow was completed, a straight edge was used to carefully scrap off and level the excess powder mounding over the top of the collection cup, as shown in Figure 33. A scale was then used to record the mass of the powder contained in the 25 cm<sup>3</sup> cup. Apparent density was then calculated using Equation 3 where  $AD$  is apparent density and  $m$  is measured mass.

$$AD = \frac{m}{25} \left[ \frac{g}{cm^3} \right] \quad (3)$$

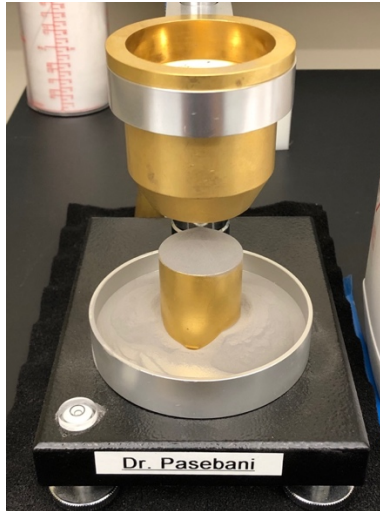


Figure 32: Metal powder filled and overflowing the collection cup



Figure 33: Levelled H13 powder in the collection cup

### 3.1.3.2 Tap Density Measurement

Tap density (TD) was collected using a 100 mL graduated cylinder and a Quantachrome Autotap machine. Test procedures followed ASTM B527 [57]. Because the apparent density was between 1-4 g/cm<sup>3</sup>, a 100 mL graduated cylinder was used in conjunction with 100  $\pm$  0.5 g of metal powder. The experimental setup is shown in Figure 34. ASTM suggests that 3000 taps is sufficient for determining tap density, but for convenience the test was left running for a few hours and when stopped had accumulated 96,990 taps.



Figure 34: Tap density experimental setup using the Quantachrome Autotap used here

### 3.2 Wrought H13

To provide direct comparison of the AM H13 samples, a purchased sample of wrought H13 was acquired from Cincinnati Tool Steel Company. The steel is manufactured via vacuum degassed tool steel ingots and hot worked for uniformity [51]. Table 4 presents the elemental analysis of H13 samples provided by Cincinnati Tool Steel. The chemistry did not exactly match the powder chemistry, but it was within ASTM standards for H13 tool steel.

Table 4: Elemental Analysis of Wrought H13 [59]

| Element | C    | Si   | V    | Cr   | Mo   | Mn   | Fe   |
|---------|------|------|------|------|------|------|------|
| Wt.%    | 0.40 | 1.00 | 1.05 | 5.25 | 1.25 | 0.40 | Bal. |

#### 3.2.1 Homogenizing Wrought H13

Prior to heat treatment the wrought H13 was homogenized to obtain a completely homogeneous microstructure. The Rapid Temp Furnace by CM Inc. pictured in Figure 35 was used to perform the homogenization and later the tempering heat treatment. Homogenization was

performed at 1050°C for two hours with a heating rate of 10°C/min. Samples were then water quenched to obtain martensitic microstructure in wrought H13.



Figure 35: Rapid Temp Furnace by CM Inc. used for homogenizing and heat treatment

### 3.3 SLM Processing Parameters

In order to achieve satisfactory material properties, the SLM processing parameters must be optimized. A matrix of varying SLM processing parameters was designed, the density of SLMed H13 was measured, and metallography was used to observe the porosity and cracks.

#### 3.3.1 SLM Matrix

A matrix of 18 potential SLM processing parameters was constructed and can be seen in Table 5. The matrix was created by varying laser speed by row and laser power by column. Layer thickness and hatch spacing were kept constant for all samples and were 50 $\mu$ m and 40 $\mu$ m, respectively. The VED of each sample is noted as the resulting value in the matrix in J/mm<sup>3</sup>. Samples were labelled according to the number noted in parenthesis.

Table 5: H13 Printing Parameters Matrix (the numbers in parenthesis are sample numbers)

| VED in SLM Process (J/mm <sup>3</sup> ) |      | Laser Power (W) |            |            |             |
|-----------------------------------------|------|-----------------|------------|------------|-------------|
|                                         |      | 152             | 177        | 203        | 228         |
| Laser Speed<br>(mm/s)                   | 100  | 760 (18)        | -          | -          | 1140.0 (17) |
|                                         | 500  | 152.0 (13)      | 177.0 (14) | 203.0 (15) | 228.0 (16)  |
|                                         | 800  | 95.0 (9)        | 110.6 (10) | 126.9 (11) | 142.5 (12)  |
|                                         | 1100 | 69.1 (5)        | 80.5 (6)   | 92.3 (7)   | 103.6 (8)   |
|                                         | 3000 | 25.3 (1)        | 29.5 (2)   | 33.8 (3)   | 38.0 (4)    |

### 3.3.2 3D Design of Test

A cylindrical specimen measuring 11.5 mm x Ø8mm was used for SLMed samples. A 3D model of the cylinder is shown in Figure 36 along with printing orientation. The ring that follows the outer diameter of the cylinder (tube looking feature in Figure 36) is included to provide initial support for the cylinder perimeter in addition to the support material pillars.



Figure 36: SLMed specimen with orientation where the Z-axis of the machine points upward through the cylinder. The ring at the bottom provides additional support during the SLM process

An ORLAS CREATOR SLM machine equipped with a software package for modelling the part on the build platform, managing printer settings, and slicing the parts into layers was used here.

After the model was sliced according to the SLM processing parameters specified, the print was started. Oxygen levels were kept below 0.1 Vol% using nitrogen to maintain an inert atmosphere. Figure 37 shows one of the prints in progress and Figure 38 shows the same specimens at the conclusion of their print once removed from the printing chamber.

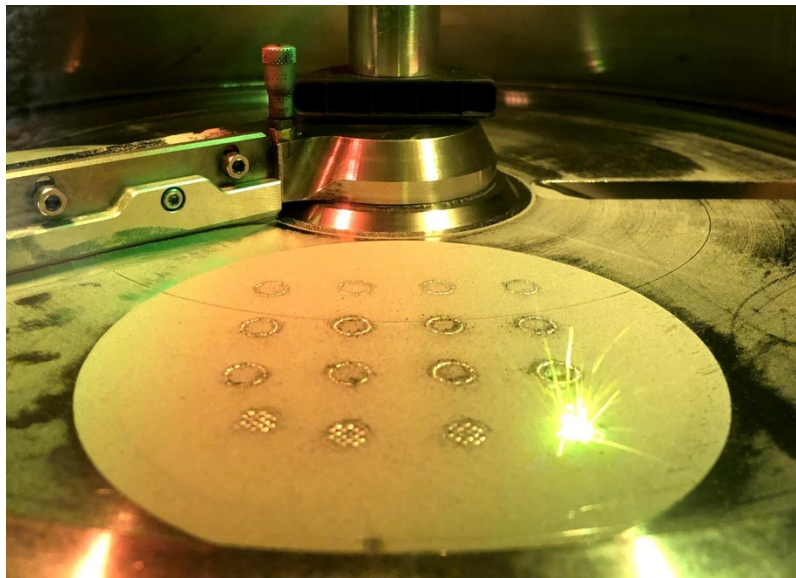


Figure 37: SLM process of H13 in an ORLAS CREATOR

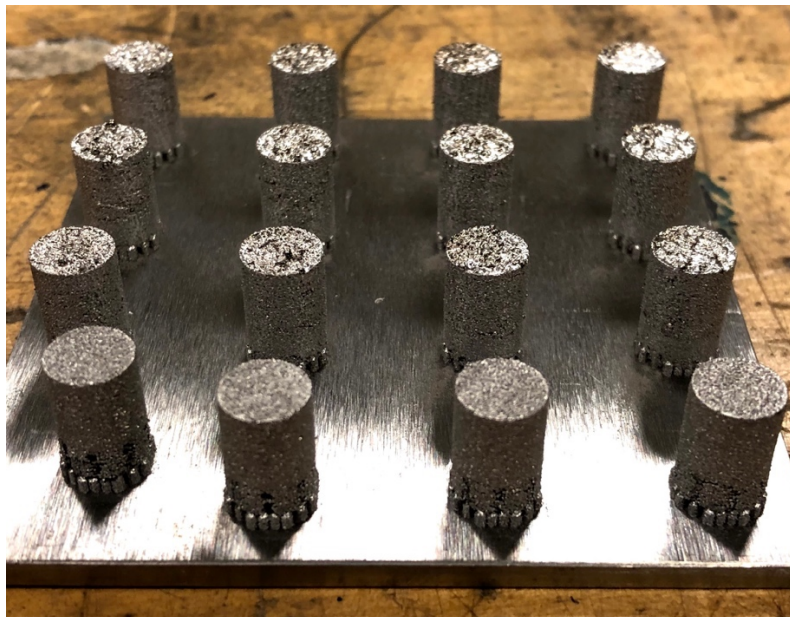


Figure 38: SLM processing parameters matrix specimens after printing showing specimens and support structure

At the conclusion of printing, samples were removed from the build platform using a chisel and hammer to remove the support structure beneath each of the cylinders. The resulting cylinders are shown in Figure 39. Excess support material was removed using pliers.

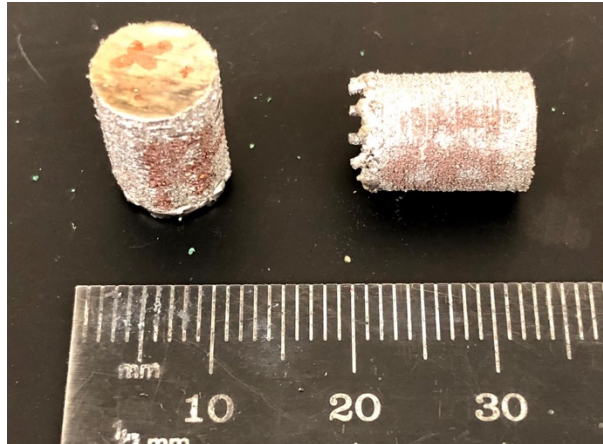


Figure 39: SLMed specimens after build plate and support structure removal

### 3.3.3 Density Measurement of SLMed H13

Archimedes density was collected for wrought and SLMed samples using Archimedes method. This was done using an Ohaus Pioneer Archimedes density measurement kit shown in Figure 40.



Figure 40: Ohaus Pioneer Archimedes density measurement kit

The Archimedes density was calculated by taking the dry mass of the sample and dividing it by the difference between the sample's dry and wet mass. The difference between the dry and wet mass results in the volume of the sample using the principle of buoyancy and the approximation that the density of water is  $1 \text{ g/cm}^3$ . The Archimedes density of each SLMed sample was compared to the average density of the wrought H13 samples to calculate a relevant density of SLMed samples.

#### 3.3.4 Microstructure Characterization

For observing grains, porosity and microstructure, wrought, SLMed, and heat-treated samples were prepared for optical microscopy using metallography technique.

Metallography was performed on eleven of the samples from the printing parameters matrix. The selected samples and corresponding VED are presented in Table 6. This made up a large range of energy densities and resulted in a wide spectrum of information to examine further.

Table 6: SLMed processing parameters samples prepared for metallography

| Sample #                    | 1    | 4    | 5    | 6    | 7    | 8     | 10    | 12    | 16    | 17     | 18    |
|-----------------------------|------|------|------|------|------|-------|-------|-------|-------|--------|-------|
| VED<br>(J/mm <sup>3</sup> ) | 25.3 | 38.0 | 69.1 | 80.5 | 92.3 | 103.6 | 110.6 | 142.5 | 228.0 | 1140.0 | 760.0 |
| Power<br>(W)                | 152  | 228  | 152  | 177  | 203  | 228   | 177   | 228   | 228   | 228    | 152   |
| Scan Speed<br>(mm/s)        | 3000 | 3000 | 1100 | 1100 | 1100 | 1100  | 800   | 800   | 500   | 100    | 100   |

### 3.3.4.1 Microscopy Sample Preparation

The first step in sample preparation was preparing cross sections of the SLMed specimens along the XZ-plane. This was done by cutting samples using a Pace Technologies PICO155P Precision Cutting Saw shown in Figure 41.



Figure 41: Pace Technologies PICO155P precision cutting saw for cross sectioning the specimens.

Once the samples were cross sectioned, they were ready for mounting into sample discs. The resin used to encapsulate the specimens was Phenolic Powder Mounting Compound by Pace Technologies. This step was done using the TP-7001B Mounting Press by Pace Technologies shown in Figure 42. The specimen was placed such that the cross sectioned portion of the specimen would be located on the face of the mounted sample disc shown in Figure 43.



Figure 42: TP-7001B Mounting Press by Pace Technologies



Figure 43: Mounted SLMed specimen ready for metallography

The final step in preparing the sample discs for metallography was grinding and polishing the faces. Grinding the samples ensured a flat surface to work with that exposed the cross sectioned face while polishing the samples eliminated any scratching on the surface that resulted from the grinding procedure. The NANO-2000T Grinder-Polisher by Pace Technologies was used to complete this process and is shown in Figure 44.



Figure 44: NANO-2000T Grinder-Polisher by Pace Technologies used for grinding/polishing mounted samples.

#### 3.3.4.2 Porosity Analysis

The porosity of each mounted and polished specimen was examined using the Zeiss Axiotron microscope, shown in Figure 45, in conjunction with the software called Amscope. Optical micrographs were obtained at 100X, 200X, 500X, and 1000X magnification containing scale bars of 400 $\mu$ m, 200 $\mu$ m, 100 $\mu$ m, and 50 $\mu$ m respectively.



Figure 45: Zeiss Axiotron optical microscope

### 3.3.4.3 Etching and Microstructural Analysis by Optical Microscopy

After optical microscopy was performed on the samples to examine porosity, they were prepared for microstructure analysis. This consisted of etching the samples and using Zeiss Axiotron optical microscopy.

A 2 Vol.% Nital solution (2 Vol.% nitric acid and 98 Vol.% ethanol) was used to expose the microstructure of the steel. The Nital was poured into a petri dish under a fume hood and the exposed face of the mounted sample was submerged. Samples were kept in the acid for varying lengths of time to expose the microstructure. Then, acid was rinsed off into a beaker with DI water. A setup of the etching is shown in Figure 46. Etched samples underwent the same procedure for optical microscopy that the porous samples underwent.

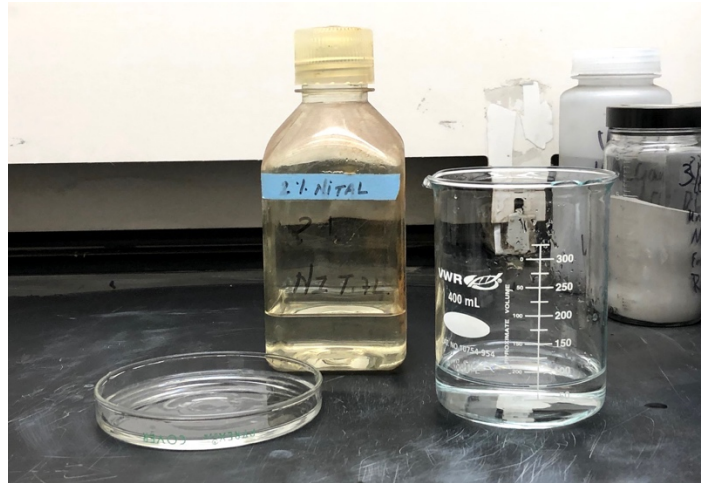


Figure 46: Etching setup beneath the fume hood

#### 3.3.4.4 Microhardness Test

Polished samples were loaded into a LECO LM 248AT microhardness tester (pictured in Figure 47) to measure the microhardness values. Vickers hardness values were recorded using a 10 second dwell time and 300 grams force. Ten random indentations were made for each specimen and the average microhardness value was reported. Figure 48 shows a sample loaded into the machine in preparation for microhardness testing.



Figure 47: LECO LM 248AT microhardness tester

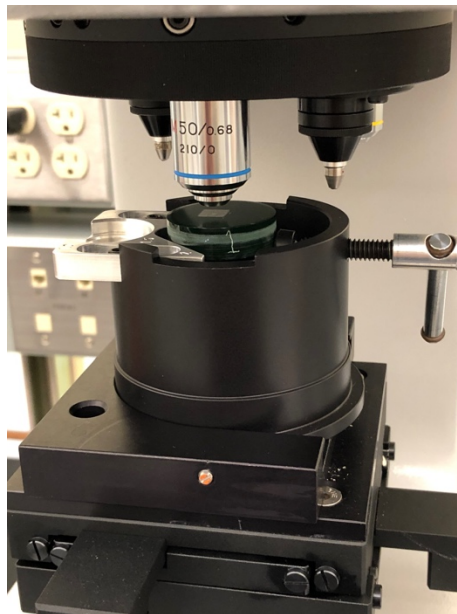


Figure 48: Sample loaded into the microhardness tester in preparation for testing

### 3.4 Tempering Heat Treatment

Tempering heat treatment was conducted on both the SLMed H13 samples and the homogenized, wrought H13 sample. Different heat treatment conditions were used to produce varying microstructures and microhardness values within the samples.

### 3.4.1 Heat Treatment Method and Groups

Heat treatment was performed in the same box furnace that homogenization was conducted. H13 wrought and SLMed samples were separated into four distinctive groups that included control, and tempered at 550°C, 600°C, and 650°C using a heating ramp rate of 10°C/min and dwell time of two hours followed by furnace cooling. The temperature profile followed for each temperature is shown in Figure 49. The above metallographic procedure was used on heat treated samples to collect optical micrographs and microhardness data.

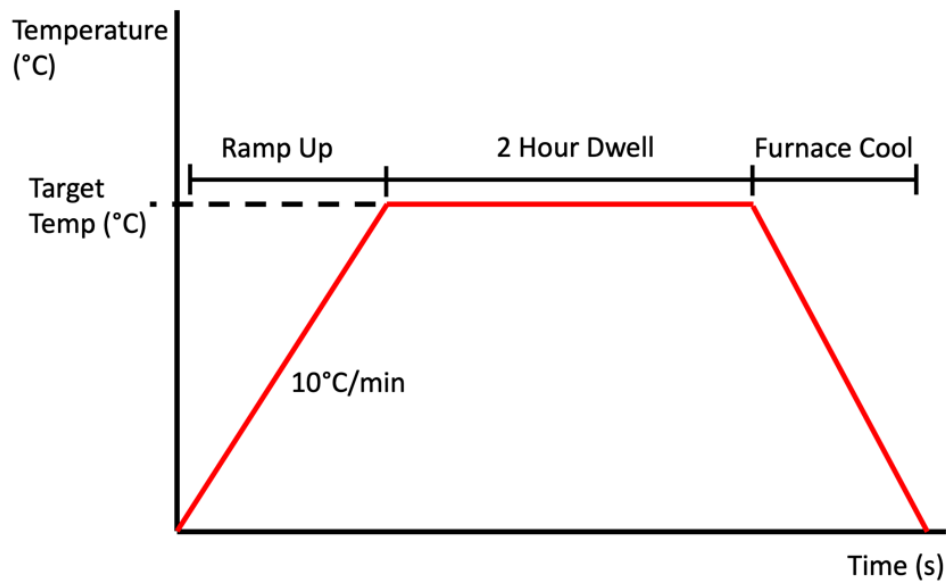


Figure 49: Temperature profile used for tempering heat treatment of H13 SLMed and homogenized H13 wrought alloy

## 4 Results and Discussion

The completion of the experimental methods yielded results pertaining to morphology, density, porosity, microstructure, and microhardness. Discussion on the findings is conducted parallel to the presentation of the data.

### 4.1 Powder Morphology

The gas-atomization process for creating spherical metal powder is not perfect, nor consistent. Many different shapes and sizes are present, as can be seen in Figure 50. Numerous particles possess satellites (when two particles are joined together). The satellites were likely attributed to the gas-atomization process where the molten metal cooled too quickly for the two particles to become completely separated. In addition, some particles show signs of having once had satellites, with only a crater remaining now after they broke apart and separated.

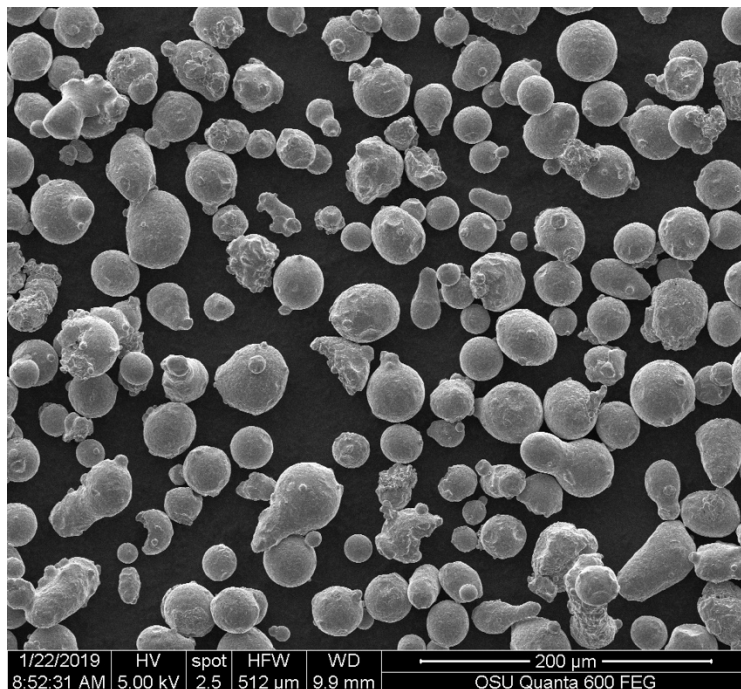


Figure 50: SEM micrograph on H13 tool steel powder gas atomized by Carpenter Technology

A higher magnification was used in the SEM micrograph shown in Figure 51. This image gives a more detailed view that shows the particles are generally smooth, but there are also some very coarse particles as well as some non-spherical particles. Small swells are visible on many of the particles. In the center of the image a particle possessing a pronounced crater is seen.

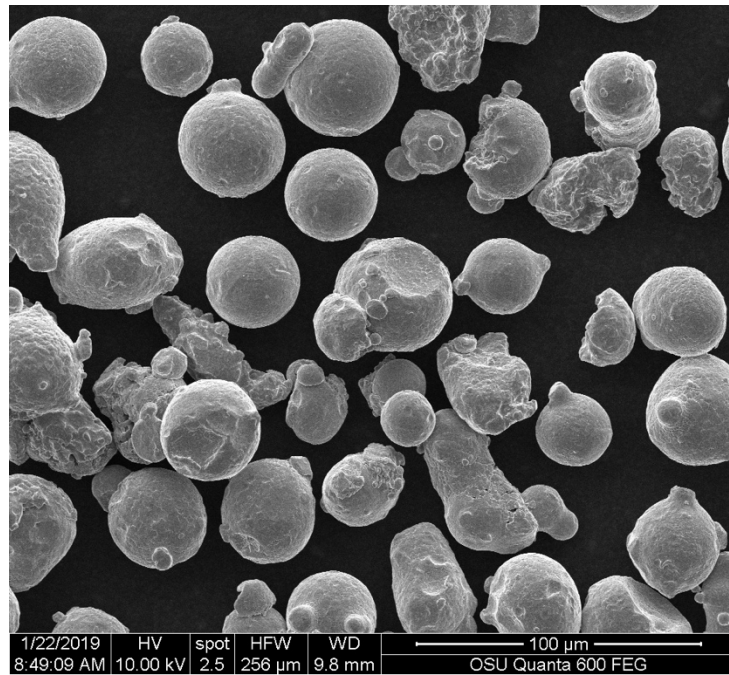


Figure 51: SEM micrograph obtained at higher magnification showing morphology of the H13 powder

#### 4.2 Particle Size Distribution

Particle size distribution was measure using the laser diffraction method (Malvern) and analysis of SEM micrographs by ImageJ. Measuring the particle size using ImageJ software is not as accurate as the laser diffraction method used. Imaging software only ever sees two dimensions of the particle, which adds uncertainty to the data. The technique of thresholding to find particle boundaries is not without error because of imperfect contrast between particles. This coupled with overlapping particles and the developed particle outlines contain a significant amount of error.

However, for comparison between the laser diffraction method and ImageJ analysis of SEM micrographs, both methods are used here.

Figure 52a-b show the boundaries discerned by ImageJ for the particles in (a) Figure 50 and in (b) Figure 51, respectively. Particles on the image boundary were omitted as they were not complete particles capable of being analyzed. The average particle size was measured to be, 37.5 $\mu\text{m}$ , which is well within the manufacturer specified range of 15-45 $\mu\text{m}$ .

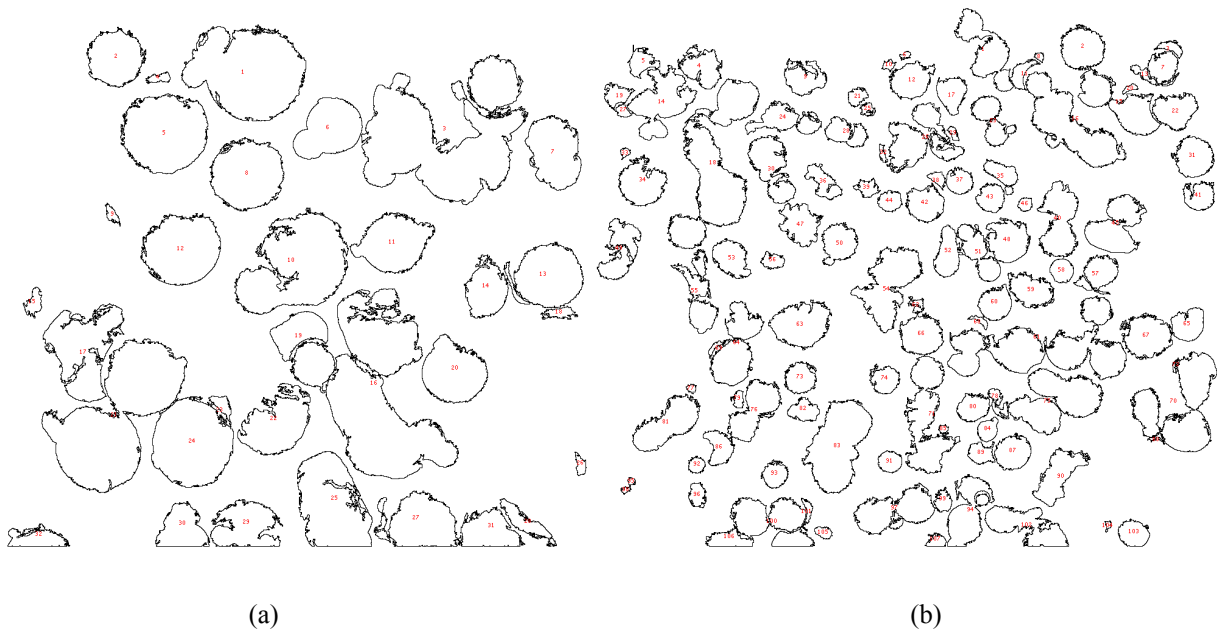


Figure 52: Discerned particle outlines using ImageJ of a (a) highly magnified micrograph and a (b) lower magnified micrograph

Using the laser diffraction method, data from 60 measurements with varying conditions were compiled to form the following results. Laser obscuration varied between 5.84% and 6.82%, with an average of 5.95%. The particle size distribution histogram is shown in Figure 53. The plot contains overlapping curves from all 60 measurements which forms a Gaussian distribution along a logarithmic axis scale. The median particle size ( $D_{50}$ ) was found to be 36.2 $\mu\text{m}$  using the laser diffraction method.  $D_{10}$  and  $D_{90}$  were found to be 25.9 and 50.4  $\mu\text{m}$ , respectively.

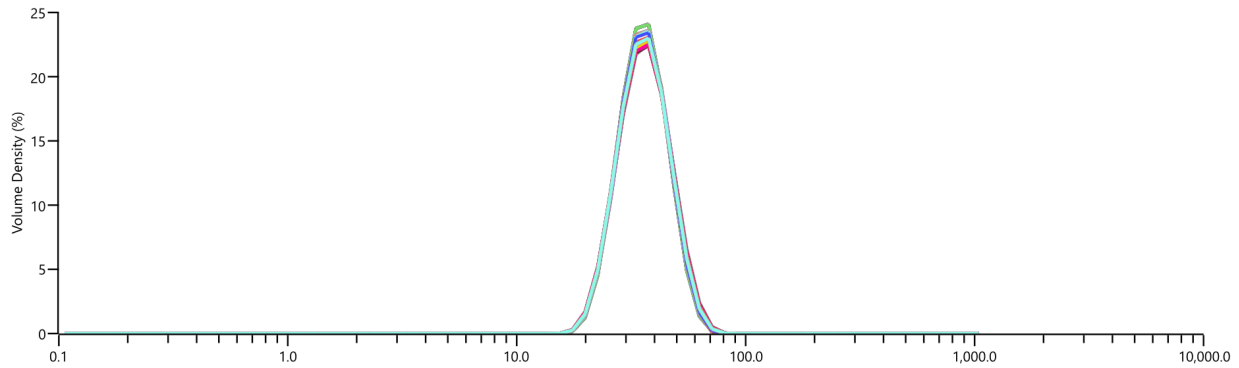


Figure 53: Particle size distribution histogram for all measurements of the H13 powder. X-axis is powder size in  $\mu\text{m}$  on a logarithmic scale

The results show that 80% of the powder falls within a range of 25.9-50.4  $\mu\text{m}$  in diameter. This information is useful for determining layer thickness in the printing process. In this case the layer thickness was set to 50 $\mu\text{m}$  because 90% of particles can fit in a single layer. If the layer thickness had been set to 25 $\mu\text{m}$  only 10% of the powder would be able to fit within a single layer.

ImageJ's value of 37.5  $\mu\text{m}$  was close to the median particle size of 36.2  $\mu\text{m}$  measured by laser diffraction methods. The imaging method returning a large diameter is explainable due to overlapping and combined particles returning larger diameters and pushing the average upward.

### 4.3 Powder Feedstock Density

The results of the apparent density and tap density measurements are in the following sections.

#### 4.3.1 Apparent Density

The resulting apparent densities from the Hall Flowmeter test are shown in Table 7. The calculated densities had an average of  $3.94 \pm 0.03 \text{ g/cm}^3$ .

Table 7: Apparent Density Data and Calculations

| Trial Number | Mass (g) | Volume (cm <sup>3</sup> ) | Apparent Density (g/cm <sup>3</sup> ) |
|--------------|----------|---------------------------|---------------------------------------|
| 1            | 99.8160  | 25.0                      | 3.9926                                |
| 2            | 98.4853  | 25.0                      | 3.9394                                |
| 3            | 98.4093  | 25.0                      | 3.9364                                |
| 4            | 98.2437  | 25.0                      | 3.9297                                |
| 5            | 98.1434  | 25.0                      | 3.9257                                |
| Average      | 98.6195  | 25.0                      | 3.9448                                |

#### 4.3.2 Tap Density

The actual mass of the powder used for the tap density measurement was 99.99 g. This value is well within the  $\pm 0.5$  g specified by ASTM. The volume of powder was challenging to read due to a developed angle as can be seen in Figure 54. Using the noted mass and the final volumetric reading of 21.0 cm<sup>3</sup>, the tap density was calculated to be 4.76 g/cm<sup>3</sup>. As expected, this is quite a bit denser than the apparent density of the powder. Specifically, the tap density of the powder is 20.7% more dense than the apparent density.

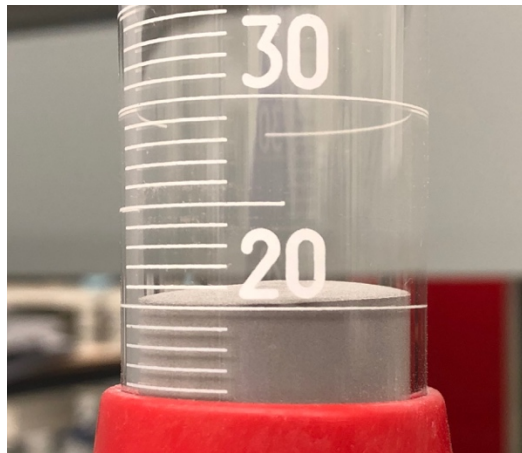


Figure 54: Profile of the H13 powder in the graduated cylinder upon conclusion of tapping

The Hausner ratio is defined by Equation 4, where AD is the apparent density and TD is the tap density; this results in a value of 1.21. A low Hausner ratio implies the powder has good flow character meaning it settles well during the spreading process associated with SLM.

$$H = \frac{TD}{AD} \quad (4)$$

#### 4.4 Manufactured Part Density

The Archimedes density for the wrought H13 samples, SLM processing parameters samples, and heat treated samples are presented in Table 8, Table 9, and Table 10, respectively.

Wrought samples, as received from the manufacturer were used to find the wrought density of H13. Table 8 shows the data from the three samples. The average wrought density used for calculating relevant density for printed samples was  $7.73 \pm 0.045 \text{ g/cm}^3$ .

Table 8: Archimedes Density of Wrought H13

| Sample Number | Archimedes Density ( $\text{g/cm}^3$ ) |                    |
|---------------|----------------------------------------|--------------------|
|               | Average                                | Standard Deviation |
| 1             | 7.7615                                 | 0.0250             |
| 2             | 7.7525                                 | 0.0014             |
| 3             | 7.6794                                 | 0.0945             |
| Average       | 7.7311                                 | 0.0450             |

The least dense sample from the printing parameters matrix was sample 1. This was expected due to the very low VED ( $25.3 \text{ J/mm}^3$ ), and in particular, the rapid scanning speed (3000 mm/s). This sample had a density of  $6.58 \text{ g/cm}^3$  and a relevant density of 85.1%. The densest sample was sample 18, which had a density of  $7.65 \text{ g/cm}^3$  and a relevant density of 99.0%. This sample did not have the highest VED, but as expected, samples with higher VED values trended upwards in density.

Table 9: Archimedes Density of SLM Processing Parameters Matrix (different power, scanning speed, and VED)

| Sample Number | VED (J/mm <sup>3</sup> ) | Archimedes Density (g/cm <sup>3</sup> ) |                    | Relevant Density (%) |
|---------------|--------------------------|-----------------------------------------|--------------------|----------------------|
|               |                          | Average                                 | Standard Deviation |                      |
| 1             | 25.3                     | 6.5790                                  | 0.5595             | 85.10                |
| 2             | 29.5                     | 6.6106                                  | 0.4998             | 85.51                |
| 3             | 33.8                     | 6.7182                                  | 0.3857             | 86.90                |
| 4             | 38.0                     | 6.7919                                  | 0.1807             | 87.85                |
| 5             | 69.1                     | 7.0904                                  | 0.2231             | 91.71                |
| 6             | 80.5                     | 7.1554                                  | 0.0576             | 92.55                |
| 7             | 92.3                     | 7.3070                                  | 0.1109             | 94.51                |
| 8             | 103.6                    | 7.4157                                  | 0.0552             | 95.92                |
| 9             | 95.0                     | 7.1423                                  | 0.1988             | 92.38                |
| 10            | 110.6                    | 7.2804                                  | 0.0700             | 94.17                |
| 11            | 126.9                    | 7.4310                                  | 0.1044             | 96.12                |
| 12            | 142.5                    | 7.4743                                  | 0.0398             | 96.68                |
| 13            | 152.0                    | 7.3867                                  | 0.0384             | 95.54                |
| 14            | 177.0                    | 7.4697                                  | 0.0801             | 96.62                |
| 15            | 203.0                    | 7.5618                                  | 0.0268             | 97.81                |
| 16            | 228.0                    | 7.5476                                  | 0.0873             | 97.63                |
| 17            | 1140.0                   | 7.6190                                  | 0.0958             | 98.55                |
| 18            | 760.0                    | 7.6543                                  | 0.0095             | 99.01                |

Sample 18's printing parameters were chosen to be the parameters used for the heat treatment samples largely due to these samples having the highest density. Five of the samples printed for heat treatment had their densities measured to represent the entire print. The least dense sample measured was sample 18-4 which had a density of 7.58 g/cm<sup>3</sup> and a relevant density of 98.1%. The densest sample was sample 18-1, which had a density of 7.66 g/cm<sup>3</sup> and a relevant density of 99.1%. The average density was lower than that of the SLM processing parameters matrix, but still held a higher density than the rest of the SLM processing parameters samples at 7.63 g/cm<sup>3</sup>. The density observed by sample 18 is within one standard deviation of the average for the additional specimens printed with sample 18's parameters, and therefore provided satisfactory results to move onto heat treatment with the samples.

Table 10: Archimedes Density of Heat Treated Samples

| Sample Number | VED (J/mm <sup>3</sup> ) | Archimedes Density (g/cm <sup>3</sup> ) |                    | Relevant Density (%) |
|---------------|--------------------------|-----------------------------------------|--------------------|----------------------|
|               |                          | Average                                 | Standard Deviation |                      |
| 18-1          | 760                      | 7.6596                                  | 0.0161             | 99.08                |
| 18-2          | 760                      | 7.6581                                  | 0.0125             | 99.05                |
| 18-3          | 760                      | 7.6120                                  | 0.0748             | 98.46                |
| 18-4          | 760                      | 7.5809                                  | 0.0120             | 98.06                |
| 18-5          | 760                      | 7.6486                                  | 0.0210             | 98.93                |
| Average       | 760                      | 7.6319                                  | 0.0273             | 98.72                |

After undergoing heat treatment, the printed and wrought samples had their densities measured. The resulting densities can be found in Table 11. “W” stands for wrought and “P” stands for printed, the number represents the temperature that the sample was heat treated at. For example, W550 means a homogenized wrought sample is tempered at 550°C and P550 means an SLMed sample is tempered at 550°C. The least dense SLMed sample was sample P650 which had a density of 7.62 g/cm<sup>3</sup> and a relevant density of 98.6%. The densest SLMed sample was sample P600, which had a density of 7.64 g/cm<sup>3</sup> and a relevant density of 98.8%. The densities of the wrought and SLMed samples are within a single standard deviation of the non-heat-treated samples, and therefore there is no evidence to suggest heat treating has any effect on the density of the steel.

Table 11: Archimedes Density of Heat Treated Samples

| Sample Number | Archimedes Density (g/cm <sup>3</sup> ) |                    | Relevant Density (%) |
|---------------|-----------------------------------------|--------------------|----------------------|
|               | Average                                 | Standard Deviation |                      |
| W550          | 7.7263                                  | 0.0130             | -                    |
| P550          | 7.6355                                  | 0.0117             | 98.76                |
| W600          | 7.7350                                  | 0.0004             | -                    |
| P600          | 7.6409                                  | 0.0097             | 98.83                |
| W650          | 7.7221                                  | 0.0162             | -                    |
| P650          | 7.6237                                  | 0.0055             | 98.61                |

#### 4.5 Microstructural Characterization

Optical microscopy was used to evaluate porosity and microstructure in both the wrought and SLMed samples.

#### 4.5.1 Porosity Analysis

Porosity of wrought and SLMed samples are analyzed using optical micrographs obtained from the as-polished surface. The darker contrast is attributed to pores within the specimen while the brighter contrast is attributed to non-porous portions of the specimen. Examples of porous samples with significant voids are shown in Figure 55a-b. The samples shown are (a) sample 1 and (b) sample 4 from the printing parameters matrix with corresponding VED of  $25.3 \text{ J/mm}^3$  and  $38.0 \text{ J/mm}^3$ , respectively. Using thresholding to distinguish between voids and material, area fraction of porosity was measured to be 43% and 27% in sample 1 (VED of  $25.3 \text{ J/mm}^3$ ) and sample 4 (VED of  $38.0 \text{ J/mm}^3$ ), respectively. This implies a 50% increase in VED led to a 16% decrease in porosity.

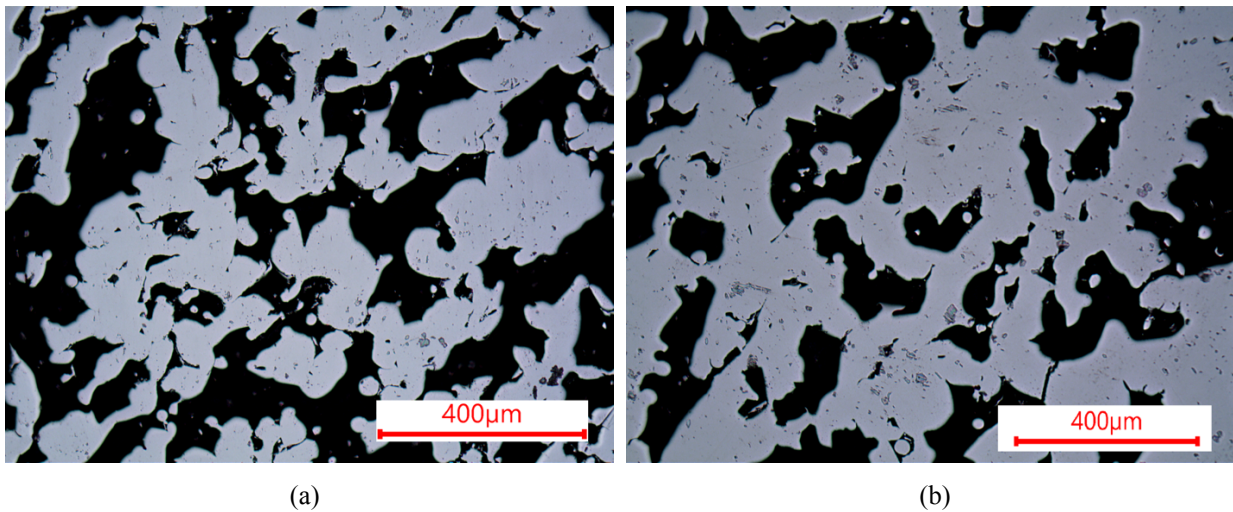


Figure 55: Optical micrograph obtained from as-polished surface of SLMed sample at (a) VED of  $25.3 \text{ J/mm}^3$  or sample 1 and (b) VED of  $38.0 \text{ J/mm}^3$  or sample 4

Optical micrograph of a less porous sample (sample 18 with VED of  $760.0 \text{ J/mm}^3$ ) is shown in Figure 56a. Additionally sample 10 with a VED value of  $110.6 \text{ J/mm}^3$  is shown in Figure 56b. Significant increases in VED for these two samples led to significant decreases in porosity because area fraction of porosity was measured to be 22% and 0.5% for sample 10 and sample 18, respectively. This shows a 21.5% decrease in porosity due to a 587% increase in VED. Low levels

of porosity were associated with high levels of VED, but the rate at which porosity declined decreased as VED was increased to higher and higher levels. Furthermore, cracks are observed in the building direction of SLMed samples at higher VED as shown in Figure 56b.

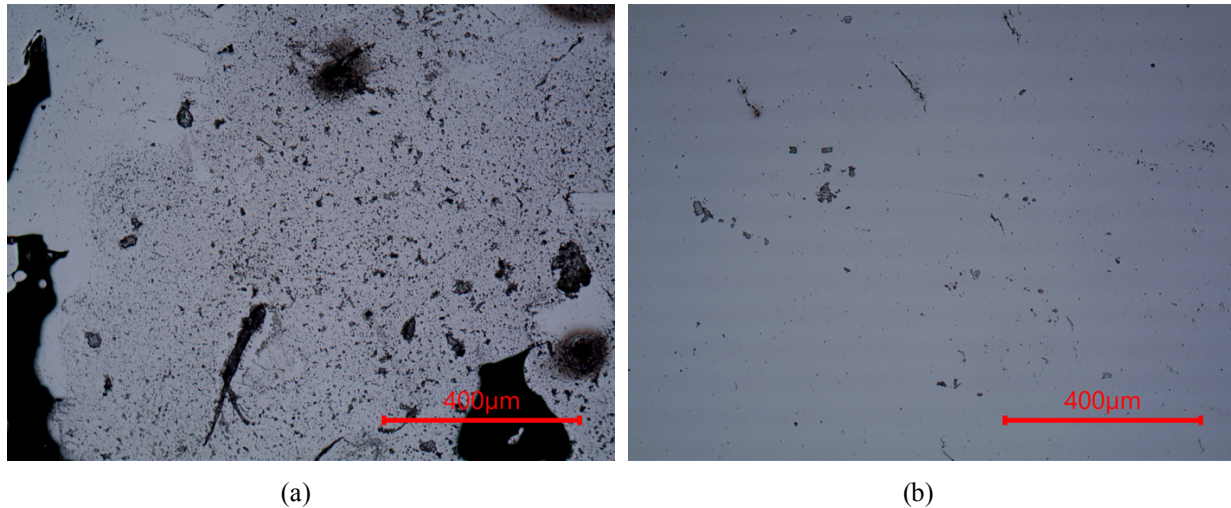


Figure 56: Optical micrograph obtained from as-polished surfaces of SLMed samples with (a) VED of  $110.6\text{J/mm}^3$  (sample 10) and (b) VED of  $760.0\text{J/mm}^3$  (sample 18)

Wrought H13 samples were examined by optical microscopy for porosity. Two optical micrographs from as-polished wrought samples can be seen in Figure 57. Figure 57 shows very few pores are visible in the specimens with only a few spots scattered about. ImageJ analysis showed very low porosity of less than 0.01%. This is expected due to the conventional manufacturing method of the wrought samples. The wrought H13 was fully melted and poured, then hot rolled into a slab, resulting in very low remaining porosity.

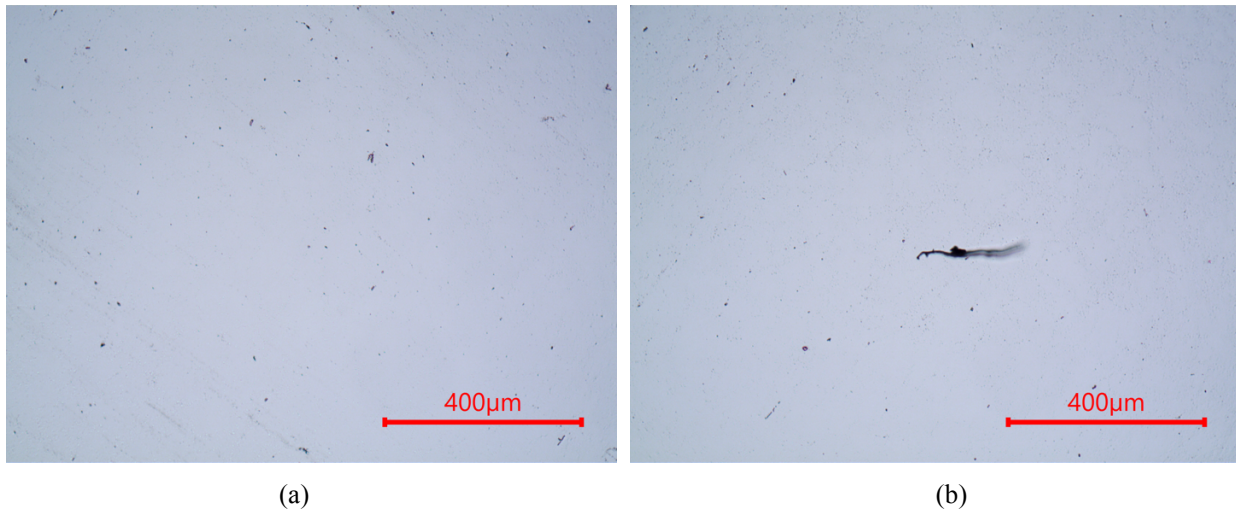


Figure 57: Optical micrographs obtained from as-polished surfaces of homogenized, wrought H13 tool steel samples

#### 4.5.2 Microstructure and Grain Analysis

A microstructure and grain analysis was conducted on SLMed samples, austenitized and water quenched samples, and wrought and SLMed samples that underwent tempering.

##### 4.5.2.1 Austenitized and Water Quenched and As-Printed SLMed

A 2 Vol.% Nital solution was used as the etchant solution to reveal martensite needles, austenite, and ferrite grain boundaries. Figure 58 shows the microstructure of austenitized and water quenched H13 tool steel with martensitic needles that were difficult to see due to the Nital solution not effectively revealing the microstructure. The high hardness (691.2 HV) supports the fine, martensitic microstructure in wrought H13 after austenitization and water quenched.

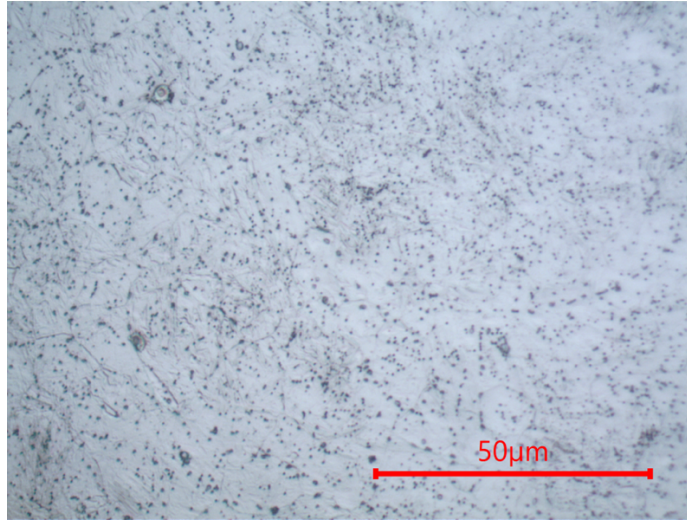


Figure 58: Optical micrograph of austenitized and water quenched H13 wrought alloy etched with 2% Nital solution

Microstructure of SLMed sample 18 H13 is shown in Figure 59. Needle martensite was revealed with the grains parallel to the build direction. Melt pools were visibly acting as boundaries between groups of martensite. Both martensite and retained austenite could be explained by the knowledge that the material undergoes extremely rapid heating and cooling during the SLM process. The martensitic microstructure, with its high dislocation density, explains the high hardness observed in sample 18 ( $708 \pm 12.63$  HV).

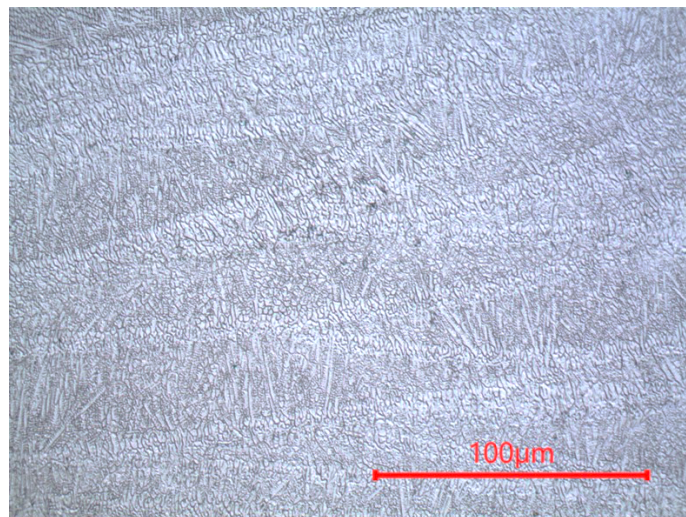


Figure 59: Optical micrograph of SLMed H13 (Sample 18 with VED of  $760.0 \text{ J/mm}^3$  and etched with 2% Nital solution)

#### 4.5.2.2 Tempered Wrought and SLMed Samples

Microstructure of austenitized and water quenched wrought H13 and SLMed H13 tool steel after tempering at 550°C and etched with Nital are given in Figure 60a-b. Needle-shaped martensite is presented, especially visible in the printed sample. The melt pool boundaries in the tempered SLMed sample are less visible than the austenitized and water quenched sample. The printed sample was approximately 65 HV harder than the wrought sample and actually increased from the water quenched sample. This is likely due to carbon in the martensite migrating to form very fine carbides within the material, and thus hindering dislocation motion within the grains [54]. Neither sample shows signs of coarse precipitates along the grain boundaries as 550°C and 1 hour did not lead to coarsening of carbides. High hardness values of  $661.66 \pm 14.52$  HV and  $728.53 \pm 28.19$  HV for wrought and SLMed tempered at 550 °C can be correlated to presence of martensite structure after tempering.

At 600°C, the tempering process is beginning to make noticeable differences in the microstructure. Figure 60c-d show both wrought and SLMed samples tempered at 600°C, respectively. Both samples revealed a fine martensitic microstructure, with precipitates found along the grain boundaries. Tempered martensite, ferrite (brighter contrast) and carbides (darker contrast and  $\text{Fe}_3\text{C}$  or cementite precipitates) were observed for both wrought and SLMed tempered at 600°C. Ferrite, a ductile material, accounts for the lowered hardness values observed in both samples (hardness values of  $616.13 \pm 27.48$  HV and  $686.79 \pm 61.02$  HV for wrought and SLMed tempered at 650 °C, respectively). Ductility is an attractive quality that increases material toughness, ideal for a fatigue inducing process such as injection molding which is one of the main applications of H13 tool steel.

At 650°C the precipitates coarsening was observed along grain boundaries, and significant density of ferrite grains were seen throughout the microstructure. This is shown for both wrought and SLMed samples after tempering at 650°C as shown in Figure 60e-f, respectively. During tempering at 650°C, carbon atoms are diffusing from martensite to form carbides. This was accompanied by formation of ferrites and carbides and led to reduction in hardness values of  $495.62 \pm 8.19$  HV and  $637.93 \pm 52.45$  HV for wrought and SLMed tempered at 650 °C, respectively. Reduction in hardness can lead to higher ductility required for excellent for wear resistance in H13 tool steel.

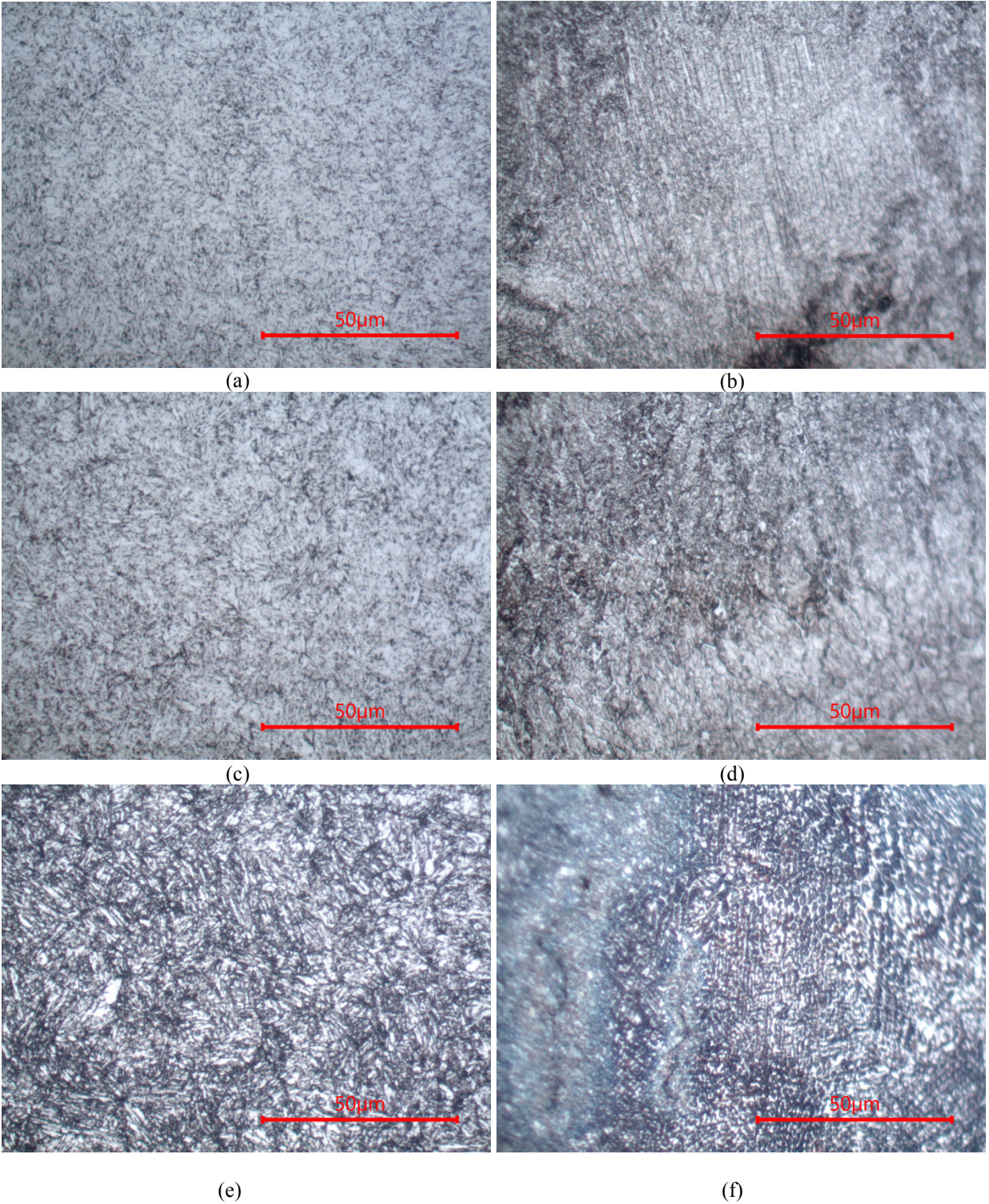


Figure 60: Optical micrographs of tempered H13 tool steel etches with 2 Vol.% Nital solution: (a) wrought and tempered at 550°C, (b) SLMed and tempered at 550°C, (c) wrought and tempered at 600°C, (d) SLMed and tempered at 600°C, (e) wrought and tempered at 650°C and (f) SLMed and tempered at 650°C

## 4.6 Mechanical Properties

The mechanical properties of the samples were evaluated by measuring microhardness data on the as-printed, austenitized and water quenched, and tempered samples.

### 4.6.1 Microhardness

Microhardness data is obtained from SLMed samples, H13 wrought samples and heat treated SLMed and wrought samples. Microhardness data is shown in Table 12. A wide range of microhardness values were observed with large standard deviations as shown in Table 12. No meaningful trends between VED and hardness data could be identified. This is attributed to the uncorrelated relationship between VED and cooling rate which was studied by Bertoli *et al.* [40] when examining varied, single-track parameters with equal VED values. Figure 61 shows five single-track SLM prints of 316L stainless steel printed with the same VED value ( $242 \text{ J/mm}^3$ ). Melt pool width is shown to be wider and more consistent at lower laser powers and scanning speeds; overall, irregular morphology appears at higher laser powers and scanning speeds.

Table 12: Microhardness data for the printing parameters matrix

| Sample             | 1     | 4     | 5     | 6     | 7     | 8     | 10    | 12    | 16    | 17    | 18    |
|--------------------|-------|-------|-------|-------|-------|-------|-------|-------|-------|-------|-------|
| Microhardness (HV) | 638.5 | 608.7 | 609.0 | 612.7 | 617.5 | 578.9 | 597.1 | 590.6 | 604.6 | 670.8 | 708.4 |
| Standard Deviation | 24.3  | 34.4  | 22.9  | 14.1  | 22.2  | 18.6  | 17.8  | 2.6   | 29.4  | 98.3  | 25.0  |

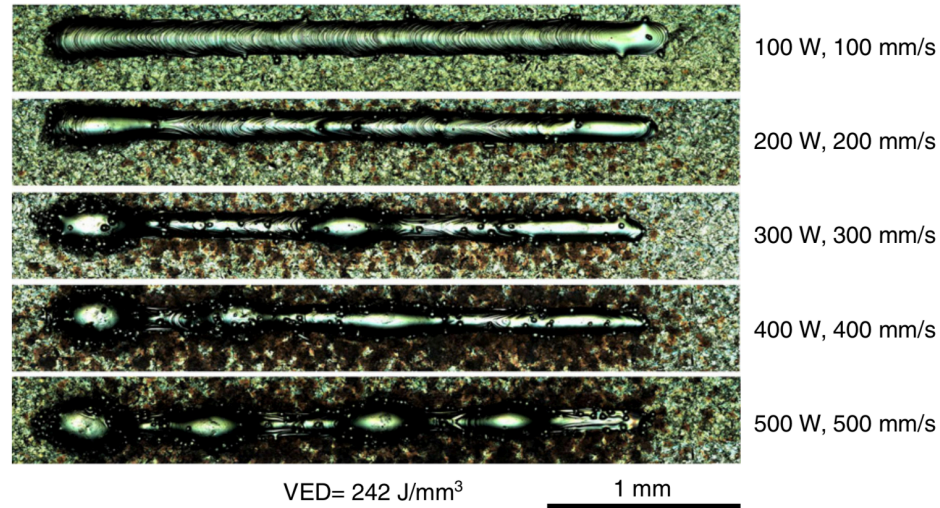


Figure 61: Five single-track SLM prints of 316L stainless steel with the same VED value (242 J/mm<sup>3</sup>). Laser power and scanning speed are shown increasing from the top the bottom of the five images [40]

Prior to heat treatment, microhardness data was collected on the as-received wrought H13 and the austenitized and water quenched sample. The results are shown in Table 13. Microhardness of as-received was measured to be very low microhardness with a very small standard deviation; 201.85±2.15 HV. This can be partially attributed to a slow cooling rate during conventional manufacturing and casting method, and partially due to hot-rolling and subsequent dynamic recrystallization and grain growth. In contrast, the austenitized and water quenched sample showed a very high hardness due to presence of martensite.

Table 13: Microhardness data of the wrought H13

| Sample             | Wrought – As Received | Austenitized and Water Quenched |
|--------------------|-----------------------|---------------------------------|
| Microhardness (HV) | 201.85                | 708.11                          |
| Standard Deviation | 2.15                  | 12.63                           |

Microhardness data of tempered H13 wrought and SLMed H13 samples after tempering at 550, 600 and 650°C are shown in Table 14.

Table 14: Microhardness data of heat treated wrought and SLMed samples at 550, 600, and 650°C

| Sample             | W550   | P550   | W600   | P600   | W650   | P650   |
|--------------------|--------|--------|--------|--------|--------|--------|
| Microhardness (HV) | 661.66 | 728.53 | 616.13 | 686.79 | 495.62 | 637.93 |
| Standard Deviation | 14.52  | 28.19  | 27.48  | 61.02  | 8.19   | 52.45  |

The plot of the data from Table 14 is also shown in Figure 62. Hardness decreased at higher tempering temperatures. Wrought samples had significantly less hard than the SLMed samples at all three tempering. Wrought samples continued to maintain lower standard deviations than those of the SLMed samples perhaps due to less porosity and more homogenized composition and microstructure. While microhardness of wrought H13 showed 500 HV after tempering at 650°C, microhardness value of SLMed H13 after tempering at 650°C was ~ 640 HV. This could be due to rapid solidification and finer microstructure in SLMed sample as compared to wrought. Presence of residual thermal stress due to rapid solidification after laser melting could lead to higher hardness in SLMed H13 compared to wrought H13 even after tempering at 650°C.

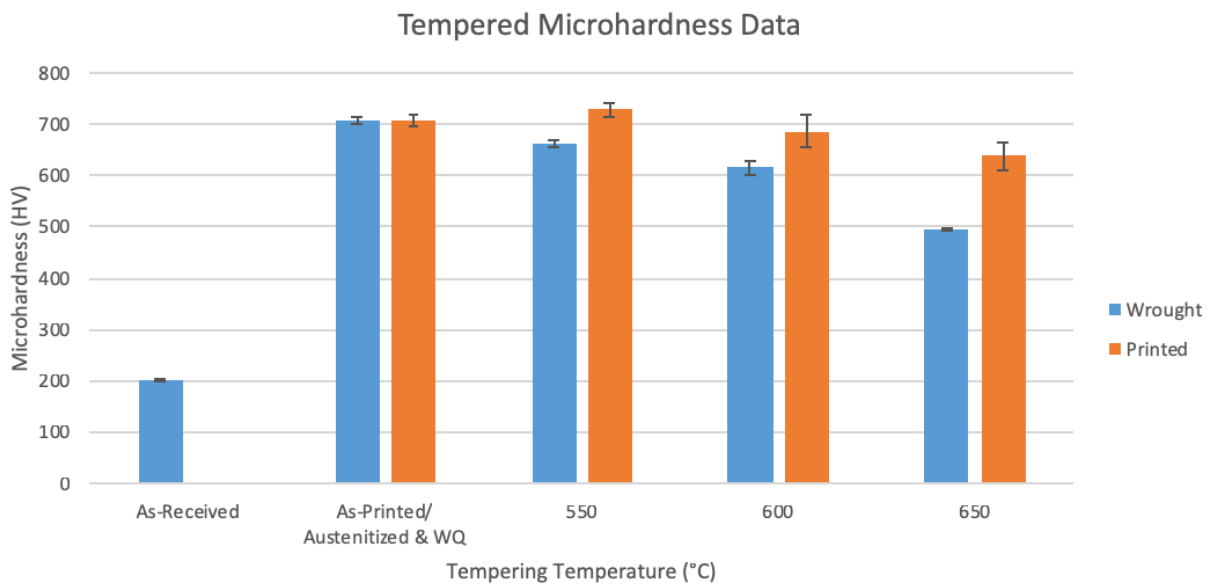


Figure 62: Microhardness data for wrought and SLMed samples at are shown at as-received, as-printed/austenitized and water quenched, 550, 600, and 650°C

## 5 Summary and Conclusions

Advances in AM, and in particular SLM, have allowed for new applications of the technology to be explored. Tooling is a field in which AM has potential to ease the manufacturing process while overcoming the design limitations and material waste associated with conventional subtractive manufacturing. Plastic injection molds are an example of a complex tool that could benefit from the SLM process. H13 tool steel is a promising molding material due to its combination of high ductility, hardness, and thermal fatigue resistance. The current knowledge on the microstructural evolutions and mechanical properties of SLM produced H13 components is limited. Therefore, this research was focused on adapting SLM process to build H13 tool steel parts, optimization of SLM processing parameters, investigation of microstructure and mechanical properties of additively manufactured parts after SLM and SLM+tempering.

H13 tool steel components with a density of ~99% were additively manufactured using the SLM process. Remained porosity of the SLMed samples was higher than remained porosity in wrought H13 tool steel samples manufactured by conventional cast and extrusion methods. After optimization of the SLM process it was found that higher values of VED correlated with higher densities and lower porosities in the SLMed parts. The highest density part (relative density 99%) with the lowest level of porosity was made with a VED of  $760 \text{ J/mm}^3$  (152 W laser power, 100 mm/s scanning speed, 40  $\mu\text{m}$  hatch spacing, and 50  $\mu\text{m}$  layer thickness). These optimal processing parameters were used to duplicate components for additional experiments that were compared with wrought H13 tool steel samples. Density, microhardness, phases and phase transformation, and microstructure of SLMed H13 was compared with those of wrought H13 tool steel parts. Furthermore, the effect of tempering at 550, 600, and 650°C (10°C/min ramp time, for two hours

followed by furnace cooling) was also examined in SLMed H13 tool steel and wrought H13 tool steel samples to enhance ductility and achieve a desired balance between hardness and ductility.

1. Tap density ( $4.76 \text{ g/cm}^3$ ) was 20.7% more dense than apparent density ( $3.94 \pm 0.03 \text{ g/cm}^3$ ) and resulted in a Hausner ratio of 1.21, indicating good powder flowability in feedstock powder.

2. Optical microscopy of polished SLM samples showed higher VED values correlated with decreased remaining porosity. The least porous SLMed sample (VED of  $760.0 \text{ J/mm}^3$ ) was measured to be less than 0.01% porous by area fraction. However, SLMed parts showed signs of cracking in the build direction leading to concerns of potential fatigue fracture in operation and plastic injection molding.

3. SLMed samples exhibited high hardness values caused by the martensitic microstructure. Austenitized and water quenched wrought H13 samples and SLMed H13 tool steel samples showed similar microhardness values of  $\sim 708 \text{ HV}$ . This means microhardness of water quenched wrought was exactly the same as SLMed sample. Therefore, the SLM process could produce the microstructure and mechanical properties equivalent to water quenched wrought H13. This can be explained by rapid solidification occurring in the SLM process. No noticeable trends between VED and microhardness values were observed in SLM process.

4. SLMed and tempered samples had the highest microhardness value of  $728 \pm 28 \text{ HV}$  at  $550^\circ\text{C}$  which was likely due to formation of very small carbides. Fine grains and high dislocation density caused during rapid solidification of SLM and presence of carbides formed during tempering could potentially hinder dislocation movement and lead to higher hardness values. At  $600$  and  $650^\circ\text{C}$  precipitates showed coarsening and more carbon was diffused from the martensite to form carbides leaving a low carbon and ductile ferritic matrix behind. The tempered microstructure of SLMed

parts resulted in significantly lower hardness values (compared to SLMed parts) due to lower dislocation density and the inclusion of ferrite.

5. The combination of hardness and ductility along with high temperature tolerance makes H13 an excellent candidate for plastic injection molds. The SLMed H13 samples provided higher mechanical properties than wrought samples. In addition, the SLM process allows for complex design features that are frequently included in mold designs such as conformal cooling channels. Concern arises when examining the density and porosity of the SLMed samples because very high levels of relative density (99.9% or greater) were not achieved, and large pores and cracks were remained in the printed parts. In operating conditions that require high thermal fatigue resistance such as in injection molding, internal cracks and porosity should be minimized and avoided as much as possible. Therefore, a detailed investigation is required to identify the mechanisms of porosity and cracks remaining in SLMed H13 tool steel parts. In order to do that a further optimization of SLM processing parameter, powder feedstock particle size distribution and modeling evolutions of porosity and cracks are required.

## 6 Current Limitations and Future Work

There are a number of possible future works associated with limitations found in this research study.

1. Processing parameters used to print H13 were not fully optimized as well as they could have been. A larger matrix of VED values could be examined, as well as varying different parameters to achieve the same VED. The effect each parameter has on the quality of printed part could be examined more closely in this situation.

2. Another area of study would be to investigate what contributes to the cracking in the build direction seen in this study. These internal cracks are the main limitation currently seen in using SLM printed molds as they would likely fail due to fatigue fracture after the cracks begin to propagate.

3. A significant portion of this study was dedicated to the hardness of the samples but further mechanical properties of SLM printed H13 could be investigated such as tensile testing and Charpy testing. This information in combination with microstructure could provide more insight into balancing hardness, strength, and ductility.

## 7 References

- [1] Goodship, V., Arburg (Firm), and Rapra Technology Limited, 2004, *Practical Guide to Injection Moulding*, Rapra Technology, Shawbury.
- [2] German, R. M., 2012, “Metal Powder Injection Molding (MIM): Key Trends and Markets,” *Handbook of Metal Injection Molding*, Elsevier, pp. 1–25.
- [3] Huang, M.-S., and Lin, C.-Y., 2017, “A Novel Clamping Force Searching Method Based on Sensing Tie-Bar Elongation for Injection Molding,” *Int. J. Heat Mass Transf.*, **109**, pp. 223–230.
- [4] Martínez-Mateo, I., Carrión-Vilches, F. J., Sanes, J., and Bermúdez, M. D., 2011, “Surface Damage of Mold Steel and Its Influence on Surface Roughness of Injection Molded Plastic Parts,” *Wear*, **271**(9–10), pp. 2512–2516.
- [5] Zhou, H., 2013, *Computer Modeling for Injection Molding Simulation, Optimization, and Control*, Wiley, Hoboken, N.J.
- [6] Chen, Z., Turng, L.-S., and Wang, K.-K., 2006, “Adaptive Online Quality Control for Injection-Molding by Monitoring and Controlling Mold Separation,” *Polym. Eng. Sci.*, **46**(5), pp. 569–580.
- [7] Mallon, J. M., and Rapra Technology Limited, 2001, *Advances in Automation for Plastics Injection Moulding*, Rapra Technology, Shrewsbury, U.K.
- [8] Xu, X., Sachs, E., and Allen, S., 2001, “The Design of Conformal Cooling Channels in Injection Molding Tooling,” *Polym. Eng. Sci.*, **41**(7), pp. 1265–1279.
- [9] Sachs, E., Wylonis, E., Allen, S., Cima, M., and Guo, H., 2000, “Production of Injection Molding Tooling with Conformal Cooling Channels Using the Three Dimensional Printing Process,” *Polym. Eng. Sci.*, **40**(5), pp. 1232–1247.
- [10] “Basics of Injection Molding Design,” 3D Syst. [Online]. Available: /quickparts/learning-center/injection-molding-basics. [Accessed: 14-Jun-2018].
- [11] “Design Tip: Using Ejector Pins Properly on Molded Parts” [Online]. Available: <https://www.protolabs.com/resources/design-tips/using-ejector-pins-properly-on-molded-parts/>. [Accessed: 14-Jun-2018].
- [12] Ribeiro, I., Peças, P., and Henriques, E., 2013, “Incorporating Tool Design into a Comprehensive Life Cycle Cost Framework Using the Case of Injection Molding,” *J. Clean. Prod.*, **53**, pp. 297–309.
- [13] Booyesen, G., De Beer, D., Truscott, M., Combrinck, J., and Mosimanyane, D., *Combining Additive Fabrication and Conventional Machining Technologies to Develop a Hybrid Tooling Approach*.
- [14] Klink, A., Arntz, K., Johannsen, L., Holsten, M., Chrubasik, L., Winands, K., Wollbrink, M., Bletek, T., Gerretz, V., and Bergs, T., 2018, “Technology-Based Assessment of Subtractive Machining Processes for Mold Manufacture,” *Procedia CIRP*, **71**, pp. 401–406.
- [15] Davim, J. P., ed., 2013, *Machinability of Advanced Materials*, ISTE Ltd/John Wiley and Sons Inc, Hoboken, NJ.
- [16] Sames, W. J., List, F. A., Pannala, S., Dehoff, R. R., and Babu, S. S., 2016, “The Metallurgy and Processing Science of Metal Additive Manufacturing,” *Int. Mater. Rev.*, **61**(5), pp. 315–360.
- [17] Mukherjee, T., Zhang, W., and DebRoy, T., 2017, “An Improved Prediction of Residual Stresses and Distortion in Additive Manufacturing,” *Comput. Mater. Sci.*, **126**, pp. 360–372.
- [18] Optomec, 2017, “The Technology Behind LENS.”

- [19] “Metal 3D Printers - Concept Laser” [Online]. Available: <https://www.concept-laser.de/en/products/machines.html>. [Accessed: 10-Jul-2018].
- [20] Swift, K. G., and Booker, J. D., 2013, *Manufacturing Process Selection Handbook*, Elsevier, Butterworth-Heinemann, Amsterdam ; Boston.
- [21] Mireles, J., Kim, H.-C., Hwan Lee, I., Espalin, D., Medina, F., MacDonald, E., and Wicker, R., 2013, “Development of a Fused Deposition Modeling System for Low Melting Temperature Metal Alloys,” *J. Electron. Packag.*, **135**(1), p. 011008.
- [22] Wu, G., A. Langrana, N., Sadanji, R., and Danforth, S., 2002, “Solid Freeform Fabrication of Metal Components Using Fused Deposition of Metals,” *Mater. Des.*, **23**(1), pp. 97–105.
- [23] Desktop Metal, 2018, “Studio System+ Printer Specifications.”
- [24] Desktop Metal, 2018, “Studio System+ Debinder Specifications.”
- [25] Desktop Metal, 2018, “Studio System+ Furnace Specifications.”
- [26] Shim, D.-S., Baek, G.-Y., Seo, J.-S., Shin, G.-Y., Kim, K.-P., and Lee, K.-Y., 2016, “Effect of Layer Thickness Setting on Deposition Characteristics in Direct Energy Deposition (DED) Process,” *Opt. Laser Technol.*, **86**, pp. 69–78.
- [27] Javidani, M., Arreguin-Zavala, J., Danovitch, J., Tian, Y., and Brochu, M., 2017, “Additive Manufacturing of AlSi10Mg Alloy Using Direct Energy Deposition: Microstructure and Hardness Characterization,” *J. Therm. Spray Technol.*, **26**(4), pp. 587–597.
- [28] Zhang, X., Li, W., Chen, X., Cui, W., and Liou, F., 2018, “Evaluation of Component Repair Using Direct Metal Deposition from Scanned Data,” *Int. J. Adv. Manuf. Technol.*, **95**(9–12), pp. 3335–3348.
- [29] Wilson, J. M., Piya, C., Shin, Y. C., Zhao, F., and Ramani, K., 2014, “Remanufacturing of Turbine Blades by Laser Direct Deposition with Its Energy and Environmental Impact Analysis,” *J. Clean. Prod.*, **80**, pp. 170–178.
- [30] Srivatsan, T. S., and Sudarshan, T. S., 2015, *Additive Manufacturing: Innovations, Advances, and Applications*, CRC Press.
- [31] Simonelli, M., Tuck, C., Aboulkhair, N. T., Maskery, I., Ashcroft, I., Wildman, R. D., and Hague, R., 2015, “A Study on the Laser Spatter and the Oxidation Reactions During Selective Laser Melting of 316L Stainless Steel, Al-Si10-Mg, and Ti-6Al-4V,” *Metall. Mater. Trans. A*, **46**(9), pp. 3842–3851.
- [32] Masmoudi, A., Bolot, R., and Coddet, C., 2015, “Investigation of the Laser–Powder–Atmosphere Interaction Zone during the Selective Laser Melting Process,” *J. Mater. Process. Technol.*, **225**, pp. 122–132.
- [33] IvánTabernero, Paskual, A., Álvarez, P., and Suárez, A., 2018, “Study on Arc Welding Processes for High Deposition Rate Additive Manufacturing,” *Procedia CIRP*, **68**, pp. 358–362.
- [34] “Selective Laser Melting Machine SLM®500 | SLM Solutions” [Online]. Available: <https://slm-solutions.com/products/machines/selective-laser-melting-machine-slmr500>. [Accessed: 19-Jul-2018].
- [35] plc, R., “Renishaw: RenAM 500Q,” Renishaw [Online]. Available: <http://www.renishaw.com/en/renam-500q--42781>. [Accessed: 19-Jul-2018].
- [36] “TruPrint Series 1000” [Online]. Available: [https://www.trumpf.com/en\\_US/products/machines-systems/3d-printing-systems/truprint-series-1000/](https://www.trumpf.com/en_US/products/machines-systems/3d-printing-systems/truprint-series-1000/). [Accessed: 19-Jul-2018].

- [37] Darvish, K., Chen, Z. W., and Pasang, T., 2016, “Reducing Lack of Fusion during Selective Laser Melting of CoCrMo Alloy: Effect of Laser Power on Geometrical Features of Tracks,” *Mater. Des.*, **112**, pp. 357–366.
- [38] Yadroitsev, I., Bertrand, P., and Smurov, I., 2007, “Parametric Analysis of the Selective Laser Melting Process,” *Appl. Surf. Sci.*, **253**(19), pp. 8064–8069.
- [39] EOS, “EOS M 400” [Online]. Available: [https://www.eos.info/systems\\_solutions/metal/systems\\_equipment/eos\\_m\\_400](https://www.eos.info/systems_solutions/metal/systems_equipment/eos_m_400). [Accessed: 27-Feb-2019].
- [40] Scipioni Bertoli, U., Wolfer, A. J., Matthews, M. J., Delplanque, J.-P. R., and Schoenung, J. M., 2017, “On the Limitations of Volumetric Energy Density as a Design Parameter for Selective Laser Melting,” *Mater. Des.*, **113**, pp. 331–340.
- [41] Sufiiarov, V. S., Popovich, A. A., Borisov, E. V., Polozov, I. A., Masaylo, D. V., and Orlov, A. V., 2017, “The Effect of Layer Thickness at Selective Laser Melting,” *Procedia Eng.*, **174**, pp. 126–134.
- [42] Telasang, G., Dutta Majumdar, J., Padmanabham, G., Tak, M., and Manna, I., 2014, “Effect of Laser Parameters on Microstructure and Hardness of Laser Clad and Tempered AISI H13 Tool Steel,” *Surf. Coat. Technol.*, **258**, pp. 1108–1118.
- [43] “Prox Dmp 320 3D Printer Technical Specifications | 3D Systems” [Online]. Available: <https://www.3dsystems.com/3d-printers/prox-dmp-320/specifications>. [Accessed: 26-Aug-2018].
- [44] “TruPrint 5000” [Online]. Available: [https://www.trumpf.com/en\\_US/products/machines-systems/3d-printing-systems/truprint-5000/](https://www.trumpf.com/en_US/products/machines-systems/3d-printing-systems/truprint-5000/). [Accessed: 26-Aug-2018].
- [45] “LASERTEC 30 SLM 2nd Gen. - ADDITIVE MANUFACTURING Machines from DMG MORI” [Online]. Available: <https://us.dmgmori.com/products/machines/advanced-technology/additive-manufacturing/powder-bed/lasertec-30-slm>. [Accessed: 26-Aug-2018].
- [46] “The Machine – ORLAS CREATOR.”
- [47] A01 Committee, *Specification for Tool Steels Alloy*, ASTM International.
- [48] 1972, “Tool Steels.”
- [49] “Effect of Heat Treatment on Microstructure and Mechanical Properties of Laser Additively Manufactured AISI H13 Tool Steel | SpringerLink” [Online]. Available: <https://link-springer-com.ezproxy.proxy.library.oregonstate.edu/article/10.1007/s11665-017-2992-0>. [Accessed: 01-Sep-2018].
- [50] Guanghua, Y., Xinmin, H., Yanqing, W., Xingguo, Q., Ming, Y., Zuoming, C., and Kang, J., 2010, “Effects of Heat Treatment on Mechanical Properties of H13 Steel,” *Met. Sci. Heat Treat.*, **52**(7–8), pp. 393–395.
- [51] Cincinnati Tool Steel Company, “AISI H13.”
- [52] Chiang, K.-A., and Chen, Y.-C., 2005, “Laser Surface Hardening of H13 Steel in the Melt Case,” *Mater. Lett.*, **59**(14), pp. 1919–1923.
- [53] Yan, J. J., Zheng, D. L., Li, H. X., Jia, X., Sun, J. F., Li, Y. L., Qian, M., and Yan, M., 2017, “Selective Laser Melting of H13: Microstructure and Residual Stress,” *J. Mater. Sci.*, **52**(20), pp. 12476–12485.
- [54] Chen, C., Yan, K., Qin, L., Zhang, M., Wang, X., Zou, T., and Hu, Z., 2017, “Effect of Heat Treatment on Microstructure and Mechanical Properties of Laser Additively Manufactured AISI H13 Tool Steel,” *J. Mater. Eng. Perform.*, **26**(11), pp. 5577–5589.
- [55] “Malvern Mastersizer 3000.”

- [56] B09.02, “ASTM B212-17 Standard Test Method for Apparent Density of Free-Flowing Metal Powders Using the Hall Flowmeter Funnel,” **02.05**.
- [57] B09.03, “ASTM B527-15 Standard Test Method for Tap Density of Metal Powders and Compounds,” **02.05**.

